

NASA TECHNICAL
MEMORANDUM

[Handwritten signature]
NASA TM X- 53629

July 3, 1967

NASA TM X-53629

SCIENTIFIC RESULTS OF PROJECT PEGASUS
INTERIM REPORT

Space Sciences Laboratory

NASA

*George C. Marshall
Space Flight Center,
Huntsville, Alabama*

N67-34548

(ACCESSION NUMBER)	<i>62</i>
(PAGES)	<i>31</i>
(NASA CR OR TMX OR AD NUMBER)	<i>31</i>

(THRU)	<i>1</i>
(CODE)	<i>31</i>
(CATEGORY)	

TECHNICAL MEMORANDUM X-53629

SCIENTIFIC RESULTS OF PROJECT PEGASUS INTERIM REPORT

Space Sciences Laboratory

George C. Marshall Space Flight Center
Huntsville, Alabama

ABSTRACT

Project Pegasus, which has the primary objective of measuring the near-earth meteoroid environment, has provided observational results far beyond the mission for which it was originally conceived. It has provided not only observational data on meteoroid punctures but also on Van Allen belt radiations, on earth albedo, on the solar constant, on orbital and gyroscopic motions of rigid bodies, on the degradation of surface coatings under space environmental conditions, on thermal control systems, and on the lifetimes of electronic components in space operations.

NASA-GEORGE C. MARSHALL SPACE FLIGHT CENTER

NASA-GEORGE C. MARSHALL SPACE FLIGHT CENTER

TECHNICAL MEMORANDUM X-53629

SCIENTIFIC RESULTS OF PROJECT PEGASUS
INTERIM REPORT

By

Space Sciences Laboratory

SPACE SCIENCES LABORATORY
RESEARCH AND DEVELOPMENT OPERATIONS

TABLE OF CONTENTS

	Page
SUMMARY	1
INTRODUCTION (Dr. George C. Bucher, Assistant Director, Space Science Laboratory)	1
METEOROID IMPACTS (Kenneth S. Clifton, Physics and Astrophysics Division, SSL)	3
METEOROID MASS FLUX (Robert J. Naumann, Physics and Astrophysics Division, SSL)	7
RADIATION MEASUREMENTS (Richard Potter, Nuclear and Plasma Physics Division, SSL)	11
THERMAL MEASUREMENTS (Charles F. Schafer, Space Thermo- physics Division, SSL)	15
Degradation of the SMA S-13 White Coating	
Louver Function	
The Micrometeoroid Detector Panels	
Thermal Control Coating Degradation Experiment	
The "Heat-of-Fusion" Sensor	
EARTH ALBEDO MEASUREMENTS (Roger C. Linton, Space Thermo- physics Division, SSL)	25
ROTATIONAL MOTION OF PEGASUS SATELLITES (Robert L. Holland Physics and Astrophysics Division, SSL)	31
RIGID BODY ROTATIONAL THEORY (Robert L. Holland, Physics and Astrophysics Division, SSL)	33
ELECTRONICS OPERATION (Harvell P. Williams, Physics and Astrophysics Division, SSL)	41
Pegasus I	
Pegasus II	
Pegasus III	
REFERENCES	46

LIST OF ILLUSTRATIONS

Figure	Title	Page
1.	Pegasus Spacecraft	2
2.	Meteoroid Flux by Month for Pegasus II and III (0.4-mm Panels).	4
3.	Meteoroid Flux by Month for Pegasus I, II, and III (0.038-mm Panels)	4
4.	Cumulative Meteoroid Penetrations by Day for Pegasus II and III (0.4-mm Panels)	6
5.	Cumulative Meteoroid Penetrations by Day for Pegasus II and III (0.038-mm Panels).	7
6.	Electron Count Rate for Path Through Anomaly for Pegasus I	12
7.	Peak and Minimum Fluxes vs. Day of the Year for Pegasus I	14
8.	Peak and Minimum Fluxes vs. Day of the Year for Pegasus II.	14
9.	Average SMA Temperatures for Pegasus I and III	15
10.	Temperature vs. Time (Pegasus I).	16
11.	$SMA \alpha_s / \xi_T$ for S-13 Coating (Pegasus I)	17
12.	Louver Blade Opening Angle vs. Time (Pegasus I)	19
13.	Internal Battery Temperature (Pegasus I)	19
14.	Detector Panel Temperature vs. Time (Pegasus I)	21
15.	Actual and Calculated Panel Temperature (Pegasus I)	22
16.	Z-93 Coating Temperature vs. Time (Pegasus II)	22

LIST OF ILLUSTRATIONS (CONCLUDED)

Figure	Title	Page
17.	α_s / ξ_T Values vs. Time (Pegasus I)	23
18.	α_s / ξ_T Values vs. Time (Pegasus II)	23
19.	Damping of Temperature Oscillations in Heat-of-Fusion Sensor Compared to Alodine Sensor (Pegasus III)	24
20.	Earth Albedo from Pegasus I Thermal Data. March 20, 1965	26
21.	Earth Albedo from Pegasus I Thermal Data. April 11, 1965	26
22.	Earth Albedo from Pegasus I Thermal Data. May 8, 1965	27
23.	Calculated Earth Albedo Correlated with Tiros IX Cloud Chart, Using Pegasus I Thermal Data. March 20, 1965	28
24.	Correlation Between Albedo and Cloud Density - Pegasus I. March 20, 1965	29
25.	Projected Orbit of Pegasus I with Calculated Albedo. April 11, 1965	30
26.	Angular Momentum Vector Motion - Pegasus I Satellite	32
27.	Geometry of the Rotating Orbit Plane Coordinate System	34
28.	Geometry of the Angular Momentum Vector Coordinate System	35
29.	Geometry of the Principal Axes Coordinate System	36
30.	Motion of the Angular Momentum Vector in the z, y Plane	39
31.	Conceptual Sketch of Possible Paths of Motion of the Angular Momentum Vector in the z, y Plane.	40
32.	Pegasus Electronic System	43

LIST OF TABLES

	Page
I. Meteoroid Flux Measurements for Pegasus Spacecraft	5
II. Range of Pegasus Temperatures	18
III. Operational Status of Electronic Subsystems for Pegasus Satellites I, II, and III	42

FOREWORD

It sometimes occurs that an experiment, planned for one specific objective, provides observational results far beyond the single-purpose mission for which it was originally conceived. Project Pegasus, which has the primary objective of measuring the near-earth meteoroid environment, is an example in case. The three satellites have now spent 65 000 hours in orbit. They have provided, and are still providing, observational data not only on meteoroid punctures but also on Van Allen belt radiations, on earth albedo, on the solar constant, on orbital and gyroscopic motions of rigid bodies, on the degradation of surface coatings under space environmental conditions, on thermal control systems, and on the lifetimes of electronic components in space operations.

Organization, development, and technical details of Project Pegasus and preliminary results of the various measurements have been published previously. The present report is an anniversary review of Pegasus results on the occasion of the second birthday in orbit of Pegasus III on July 30, 1967. It was written by those who have reduced, analyzed, and interpreted the measured data during these past two years.

Ernst Stuhlinger,
Director. Space Sciences Laboratory

TECHNICAL MEMORANDUM X-53629

SCIENTIFIC RESULTS OF PROJECT PEGASUS
INTERIM REPORT

SUMMARY

Project Pegasus, which has the primary objective of measuring the near-earth meteoroid environment, has provided observational results far beyond the mission for which it was originally conceived. It has provided not only observational data on meteoroid punctures but also on Van Allen belt radiations, on earth albedo, on the solar constant, on orbital and gyroscopic motions of rigid bodies, on the degradation of surface coatings under space environmental conditions, on thermal control systems, and on the lifetimes of electronic components in space operations.

INTRODUCTION

The purpose of this report is to present the latest results from the three Pegasus satellites. Pegasus I was launched on February 16, Pegasus II on May 25, and Pegasus III on July 30, all during the year 1965. The three Pegasus satellites have been transmitting valuable data continuously since their launch dates; the most current results from the reduction and evaluation of these data are described in this report.

The Pegasus program was managed by the Office of Advanced Research and Technology in NASA Headquarters; project management was performed by the Marshall Space Flight Center (MSFC). Details on the history, management, and operation of Project Pegasus are given in the First Summary Report [1], which also describes the structural and systems design of the Pegasus spacecraft, as well as the characteristics of the scientific experiments. This report will not repeat that information; therefore, the reader should refer to the First Summary Report [1] if details are desired.

The configuration of the Pegasus spacecraft is shown in Figure 1. This illustration depicts some of the components mentioned in later sections of this

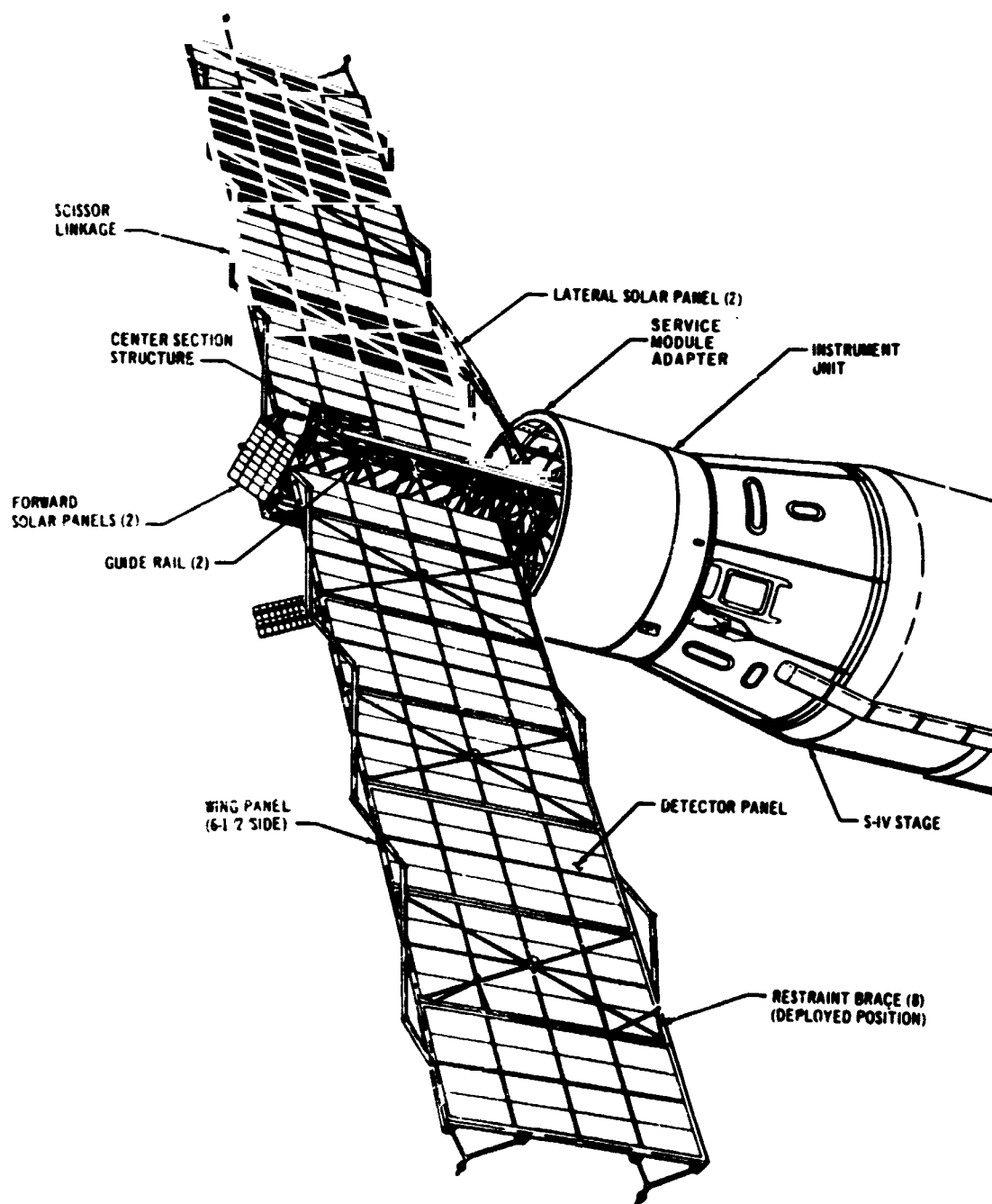


FIGURE 1. PEGASUS SPACECRAFT

report. The total meteoroid detector area, consisting of both sides of the wing panels, is about 200 m². Of this area, the 0.038-mm detectors comprise 8 m², the 0.2-mm detectors comprise 17 m², and the 0.4-mm detectors comprise 175 m². The component sections of this report were written by members of the Space Sciences Laboratory of MSFC. The authors have been continuously involved in the reduction and evaluation of Pegasus data. The report not only presents the direct observational data received from the three Pegasus satellites but also summarizes theoretical work which is related to the evaluation and analysis of Pegasus data. (See Meteoroid Mass Flux and Rigid Body Rotational Theory.) This document is an interim report on the scientific results of Project Pegasus. A more comprehensive report will be issued after all data have been received and evaluated. Present plans call for the three Pegasus spacecraft to continue operating until October 1, 1967.

METEOROID IMPACTS

Based upon the evaluation of data available in early May 1967, the three Pegasus spacecraft have recorded a combined total of 1997 meteoroid penetrations on the three panel thicknesses during their lifetimes in orbit. The 0.4-mm panels on all spacecraft have recorded a total of 392 penetrations in 94 801 m²-day for a flux of 0.0041 penetration/m²-day; the 0.2-mm panels have recorded 61 penetrations in 3512 m²-day for a flux of 0.017 penetrations/m² day; and the 0.038-mm panels have recorded 1544 penetrations in 9284 m²-day for a flux of 0.166 penetration/m²-day. The over-all penetration rates are broken down by satellite in Table I; the flux values shown are observed values uncorrected for earth shielding and other factors.

It may be seen that the penetration rates for the 0.4-mm panels on Pegasus II and III agree as closely as do the 0.038-mm panels on all three spacecraft, and these results may be combined for further analyses. The four penetrations recorded by the 0.4-mm panels of Pegasus I preclude the value of this satellite in further analyses, although the observed flux is within reasonable statistical bounds with Pegasus II and III.

In Figures 2 and 3, the meteoroid penetration data for the 0.4-mm panels of Pegasus II and III and for the 0.038-mm panels of Pegasus I, II, and III are displayed on a monthly basis. The data were collected over the entire lifetimes of the spacecraft. Error bars are included to denote a 1 σ deviation from the observed flux.

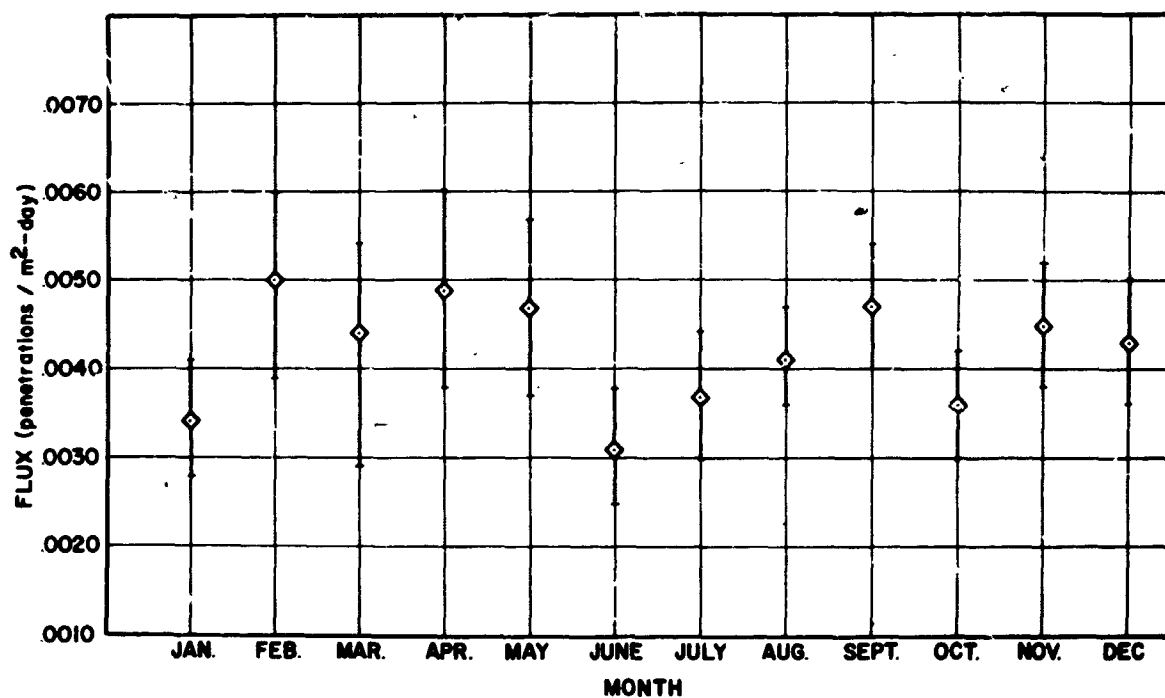


FIGURE 2. METEOROID FLUX BY MONTH FOR PEGASUS II AND III
(0.4-mm PANELS)

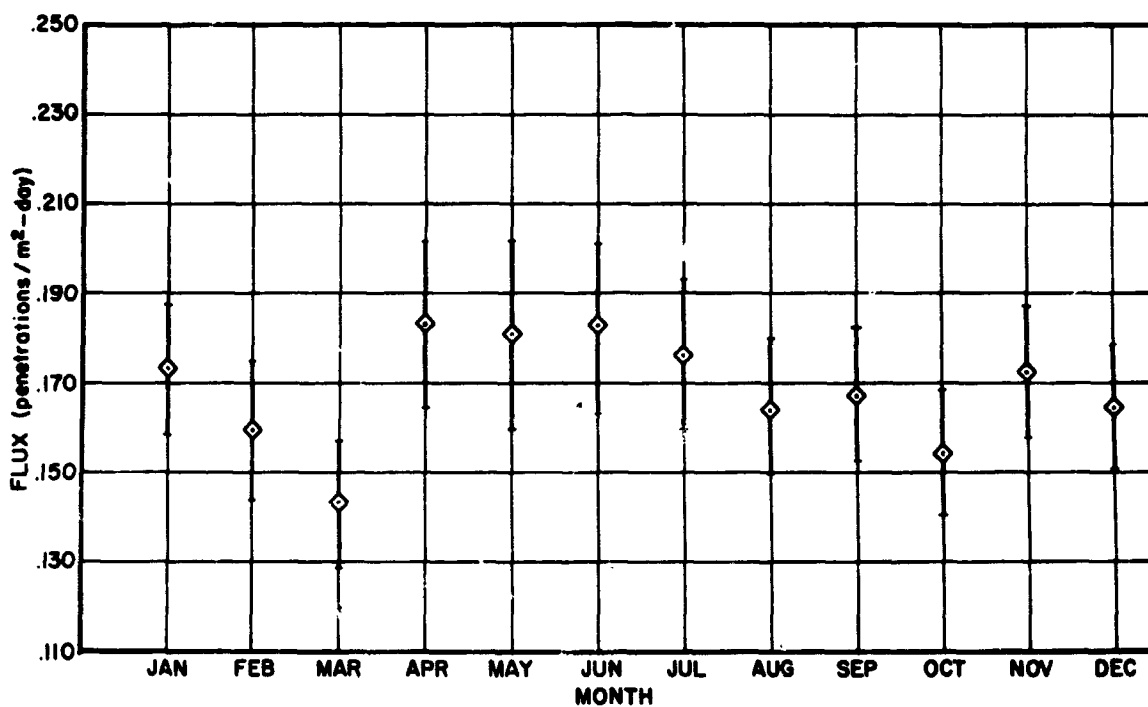


FIGURE 3. METEOROID FLUX BY MONTH FOR PEGASUS I, II,
AND III (0.038-mm PANELS)

In Figures 4 and 5 the numbers of recorded penetrations versus the days of the year are portrayed for the 0.4-mm and 0.038-mm panels of Pegasus II and III. In these illustrations the observed number of events is compared with the expected number which was calculated on the basis of the active panel area for that particular day. Once again, the data were collected over the entire lifetimes of the spacecraft. On those days for which the expected number of penetrations is zero, the area is such that less than 0.5 penetration for that day is expected. Heavy concentrations of events are of particular interest when related to known meteor showers. It may be noted from the illustrations, however, that only two such concentrations occur in which the number of observed penetrations exceeds the expected number by any substantial margin during the period of a meteor shower. The 0.038-mm panels recorded 142 penetrations during the Taurids when 128 were expected, and the 0.4-mm panels recorded 13 penetrations during the Leonids when 6 were expected. However, such concentrations may be purely statistical, as variations exceeding 2σ and 3σ limits are occasionally expected on statistical grounds (see Table I).

TABLE I. METEOROID FLUX MEASUREMENTS FOR PEGASUS SPACECRAFT

	Thickness of Detector Panel		
	0.038 mm	0.2 mm	0.4 mm
Pegasus I			
Area-Time ($\text{m}^2\text{-day}$)	1720	248	1925
Penetrations	273	8	4
Flux (penetrations/ $\text{m}^2\text{-day}$)	0.159	0.032	0.0021
Pegasus II			
Area-Time ($\text{m}^2\text{-day}$)	3520	2466	46 846
Penetrations	568	38	189
Flux (penetrations/ $\text{m}^2\text{-day}$)	0.161	0.015	0.0042
Pegasus III			
Area-Time ($\text{m}^2\text{-day}$)	4044	798	46 030
Penetrations	703	15	189
Flux (penetrations/ $\text{m}^2\text{-day}$)	0.174	0.019	0.0041

(observed flux values are uncorrected for earth shielding)

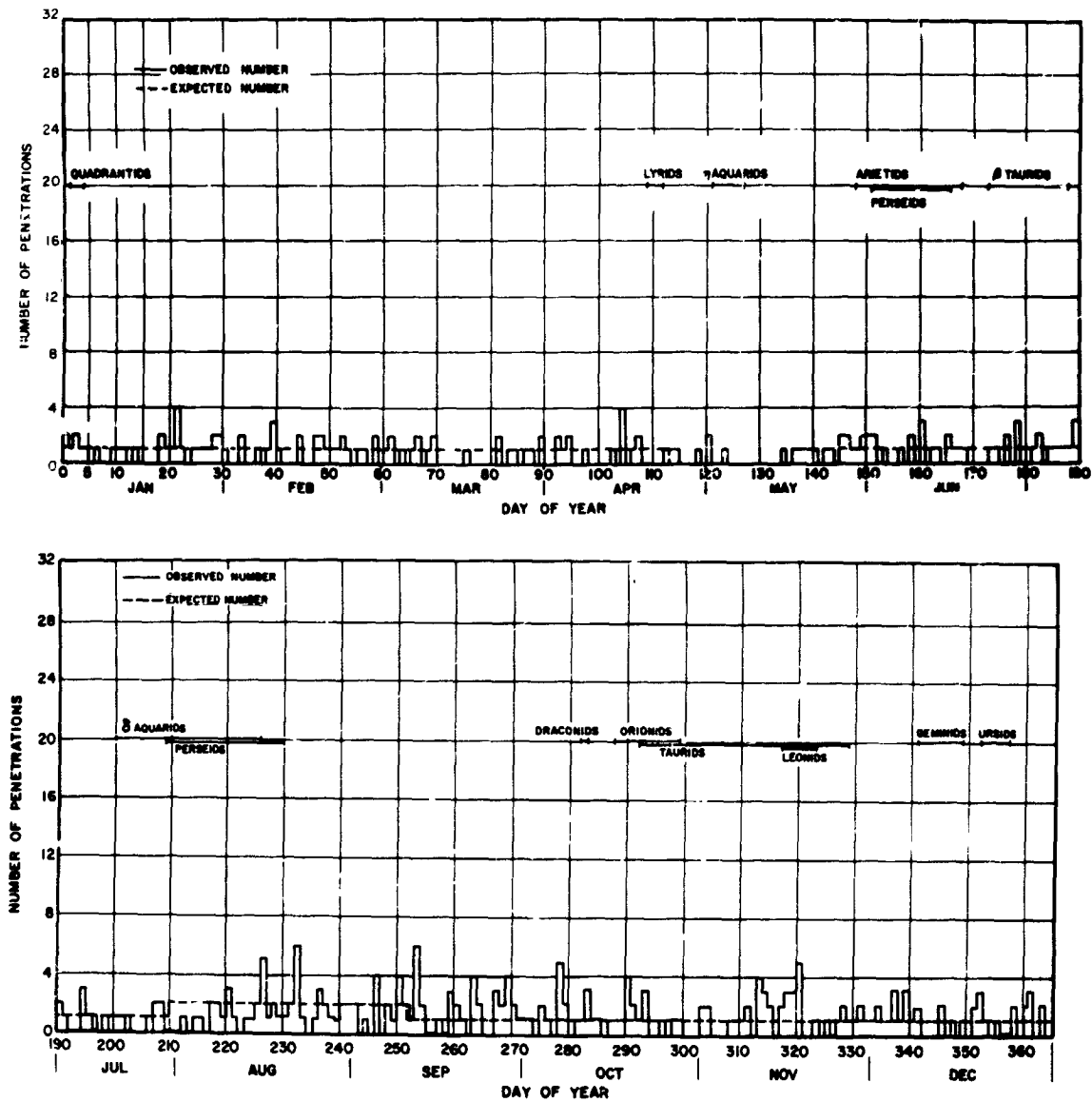


FIGURE 4. CUMULATIVE METEOROID PENETRATIONS BY DAY FOR PEGASUS II AND III (0.4-mm PANELS)

A number of other analyses, particularly directional and positional analyses, are being conducted at present. They involve small deviations from expected results and require considerable data to substantiate such deviations. The analyses are still inconclusive at this writing.

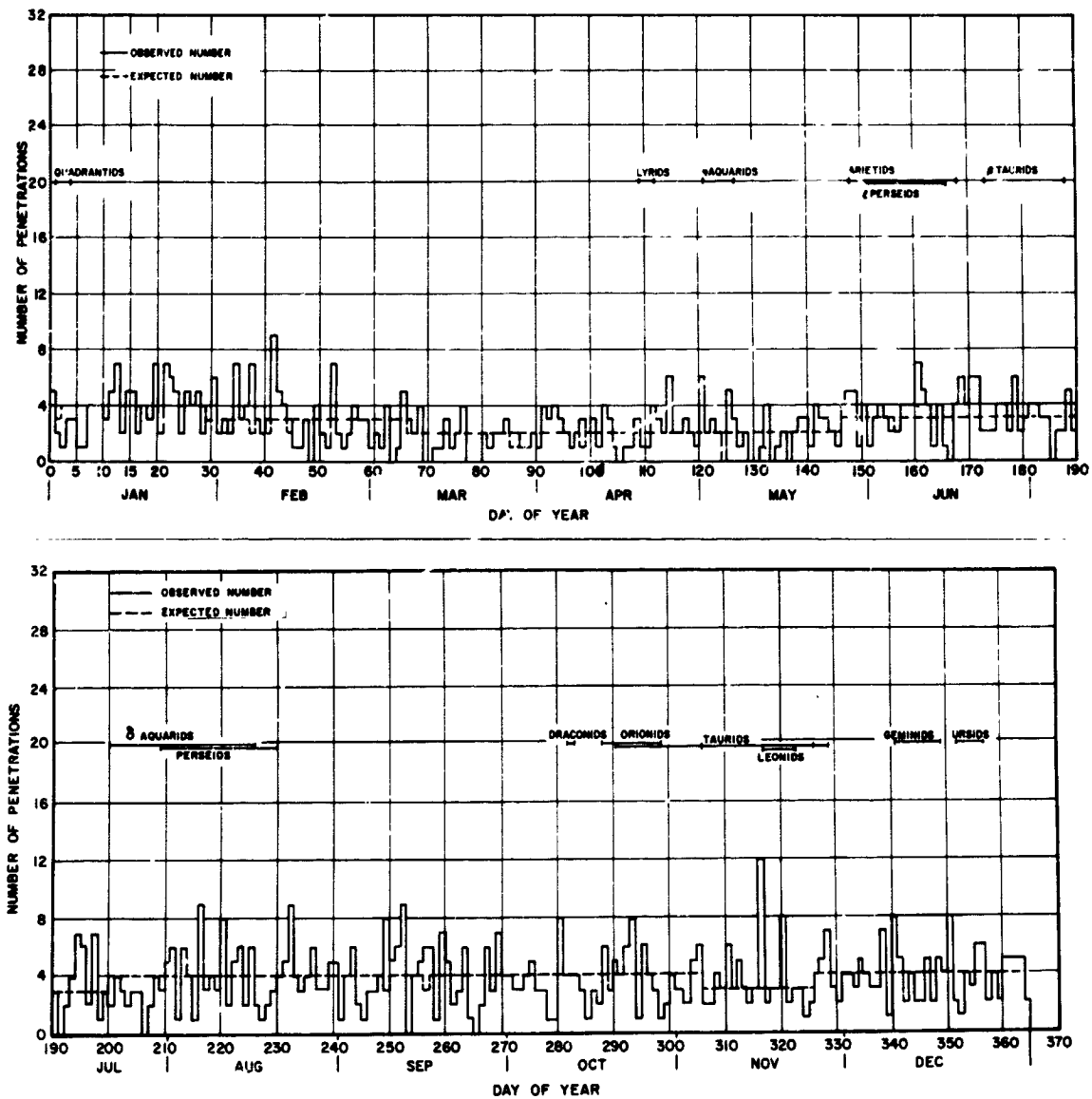


FIGURE 5. CUMULATIVE METEOROID PENETRATIONS BY DAY FOR PEGASUS II AND III (0.038-mm PANELS)

METEOROID MASS FLUX

The Pegasus meteoroid experiment was designed to give directly a penetration flux in three thicknesses of aluminum. This obviously is the item of primary importance for determining the amount of meteoroid protection

needed for a particular mission. However, to compare such measurements with other measurements such as radar or optical observations of meteor entry, it is desirable to interpret the penetration measurements in terms of a mass flux. It becomes necessary to introduce a penetration equation to relate the thickness of material penetrated T , to the mass m , velocity v , density ρ , and impact angle θ of the meteoroid. Such an equation must be empirical and the form assumed is $T = k \rho^\alpha v^\beta m^\gamma (\cos \theta)^\delta$ where k , α , β , γ and δ are constants to be determined experimentally. The mass required to perforate a given detector depends on thickness of the detector as well as the density, velocity, and angle of impact, and is denoted $m(T, \rho, v, \theta)$. Obviously, any mass larger than this will also penetrate. The penetration rate observed $\phi(T)$ for an isotropic meteoroid distribution may be expressed by

$$\phi(T) = \int_{2\pi} d\Omega \int_0^\infty d\rho \int_0^\infty dv \int_{m(T, \rho, v, \theta)}^\infty dm \cos \theta n_\rho(\rho) n_v(v) n_m(m)$$

where $n_\rho(\rho)$ and $n_v(v)$ are the normalized density and velocity probability density functions, and $n_m(m)$ is the directional mass flux distribution function such that $n_m(m) dm$ is the number of meteoroids with mass between m and $m + dm$ within unit solid angle incident on unit area in unit time.

It is convenient to introduce a cumulative mass flux

$$N(m) = \pi \int_m^\infty n_m(m) dm$$

where $N(m)$ is the number of meteoroids with mass m or greater encountering a flat, randomly oriented unshadowed surface of unit area in unit time. This is the quantity generally reported in other measurements. It is also convenient to specify a characteristic mass m_c for a particular detector which is defined as the mass required to perforate the detector for a meteoroid having average density, average velocity, and normal incidence. A relation between the observed penetration frequency, $\phi(T)$, and the encounter frequency for meteoroids with mass characteristic to that detector, $N(m)$, can be shown to be [2]

$$\phi(T) = \frac{N(m_c)}{(1 + \delta\lambda/2\gamma)} \frac{\langle \rho^{\alpha\lambda/\gamma} \rangle}{\langle \rho \rangle^{\alpha\lambda/\gamma}} \frac{\langle v^{\beta\lambda/\gamma} \rangle}{\langle v \rangle^{\beta\lambda/\gamma}}$$

where

$$\lambda = - \left(\frac{d \log N(m)}{d \log m} \right) m_c .$$

The bracket $\langle \rangle$ denotes the average of the quantity enclosed. To evaluate these averages, the density distribution $n_\rho(\rho)$ and the velocity distribution $n_v(v)$ must be known. A range of values for the exponents have been found by experimentation and theoretical considerations to be:

$$\alpha = 0 - 1/3$$

$$\beta = 1/2 - 1$$

$$\gamma = 1/3 - 19/54$$

$$\delta = 2/3$$

$$\lambda = 0.3 - 1.4 .$$

Recent work with porous projectiles with densities down to 0.7 gm/cm³ and computations [3] using equation of state for porous aluminum with bulk densities of 0.44 gm/cm³ indicates that the penetration for a given mass of material is practically independent of density for the range 0.44-2.7 gm/cm³. Taking $\alpha = 0$ sets the ratio of averages involving densities to unity. The largest value that could reasonably be expected for $\alpha\lambda/\gamma$ is about 1. This value also would set the ratio of averages to unity. For any reasonable value of α and distribution $n_\rho(\rho)$ the density term will range from 0.9 to 1.0. Thus the fact that distribution of densities is not well known is relatively unimportant.

The exponent in the velocity term, $\beta\lambda/\gamma$ will be approximately 2. The velocity distribution is not well known, but a reasonable range of values for the ratio of averages arising from the velocity distribution is 1.0 to 1.2 with an upper limit of 2. This latter value is obtained by assuming a most unreasonable velocity distribution, i. e., a bimodal distribution with 77 percent at 11 km/sec and 23 percent at 72 km/sec to give an average velocity of 25 km/sec.

It may be seen that effects from density and velocity distributions tend to counteract one another and to a good approximation may be ignored. The only significant factor that makes the encounter frequency differ from the penetration frequency is the term $1/(1 + \delta\lambda/2\gamma)$ which accounts for the decrease in penetrating ability of meteoroids with increasing obliquity of impact. This factor is approximately 0.5 which means that only half the meteoroids with

mass sufficient to penetrate at normal incidence at average velocity will actually penetrate because of their obliquity.*

Having determined the relation between observed penetration frequency and mass flux, the remaining task is to determine the mass characteristic to each detector thickness. Estimates of this characteristic mass can be made by extrapolating various empirical penetration formulas to the average meteoroid velocity, but because of the complex structure of the Pegasus detectors, penetration formulas developed for semi-infinite targets or for single plate targets cannot be relied upon. Considerable effort was expended in calibrating the actual Pegasus detector panels using the hypervelocity ranges at Hayes International [4], North American [5], and Illinois Institute of Technology Research Institute [6]. The procedure employed in the tests was to select a projectile size and vary the impact velocity to determine the velocity that just causes perforation [7]. This is repeated for several projectile sizes resulting in a plot of perforation velocity as a function of mass. This plot using log-log scales is extrapolated on a straight line to the average meteoroid velocity, taken to be 25 km/sec. The resulting mass is the characteristic mass for the detector.

For the 0.02-cm and 0.04-cm Pegasus detectors the particle sizes ranged from 130μ to 436μ diameter spheres. Perforation velocities were determined from 4 to 7 km/sec. The projectile materials were styrene-divinyl benzene ($\rho = 0.9 \text{ g/cm}^3$) and borosilicate glass ($\rho = 2.2 \text{ g/cm}^3$). Little if any difference could be determined between the two materials when compared on the basis of mass, and in light of other evidence of the fact that projectile material is unimportant in the density range of interest, no adjustment was made for density.

The thinnest target was calibrated using the same projectile materials but with sizes ranging from 70μ to 23μ and velocities ranging from 3 to 18 km/sec. Unfortunately these high velocities could not be obtained with projectiles large enough to perforate the thicker targets.

* An equivalent way of expressing this would be to define the characteristic mass as that mass that would just penetrate with average velocity and with average angle of impact, which happens to be 45 degrees for an isotropic distribution. With this definition, the encounter frequency will be almost the same as the perforation frequency, but the mass characteristic to the detector is larger. Since it is convenient to perform calibration shots at normal impact, the original definition of characteristic mass is preferred.

All calibration tests were performed on small samples of detector which were not electrically operative. Perforation was established by sensing a rear impact flash through the foam backing. All but a thin (several millimeter) layer of foam had been removed. This was the same criteria as was used in the acceptance tests of these Pegasus detectors prior to flight in which the detection probability had been established on the basis of several hundred shots as the ratio of the number of detectable signals to rear impact flashes. The data had already been adjusted by this factor (which is approximately 0.85). Therefore, it is reasonable to calibrate according to this criteria.

The characteristic masses determined from these tests are:

Detector	Characteristic Mass	Penetration Rate $\phi(T)$
0.04 cm	9.5×10^{-7} gm	0.00706/m ² day
0.02 cm	1.6×10^{-7} gm	0.0305/m ² day
0.0038 cm	1.3×10^{-8} gm	0.273/m ² day

The penetration rate values in the above table were corrected for earth shielding. The listed values represent the flux without the influence of the earth's shadow. The mass flux, i. e., the number per unit area-time with mass m or greater encountering a surface unshadowed by the earth is given by $\log N(m) = -0.1407 (\log m)^2 - 2.742 \log m - 13.316$ (no./m² day) for the interval $-9 \leq \log m \leq -6$.

RADIATION MEASUREMENTS

Each of the three Pegasus satellites is equipped with a two-channel radiation spectrometer. Each detector is a 2π solid angle device for measuring trapped electrons with a minimum of proton background. Channel 1 of the spectrometers on Pegasus I and II has a threshold of 0.5 MeV; the second channel gives a count rate of electrons with energies above 2 MeV. The count rate output is sampled every five minutes. Many radiation spectrometers flown today have more than thirty channels; the two-channel spectrometer on the Pegasus satellites was obviously not a main experiment but rather a house-keeping measurement. The purpose of the electron measurement was to determine the electron environment encountered by the meteoroid detector panels. It was feared that electrons would be deposited in the dielectric material in

great enough numbers to cause a breakdown which would erroneously indicate a meteoroid impact. Analysis of the radiation data and meteoroid data has proven that radiation did not cause spurious meteoroid counts.

All of the Pegasus satellites pass through the South Atlantic anomaly of the earth's magnetic field. The South Atlantic anomaly is the region where the Van Allen radiation belts dip closest to the earth, and, therefore, the region where particles, through interactions with the atmosphere, are lost from the belts. The radiation belts are reducing in electron intensity as Starfish electrons (electrons placed in the belt by high altitude nuclear explosions) are dumped in the anomaly region. Figure 6 shows the path of Pegasus I with a typically high count rate in the anomaly. Several satellites with charged particle detection systems more sophisticated than Pegasus have recorded data in this region. All of these satellites except Pegasus had relatively short lifetimes. There is an overwhelming problem in obtaining an exact flux reading from two different satellites by different investigators. Therefore, a long-term investigation of the South Atlantic anomaly had not been successfully completed before Pegasus.

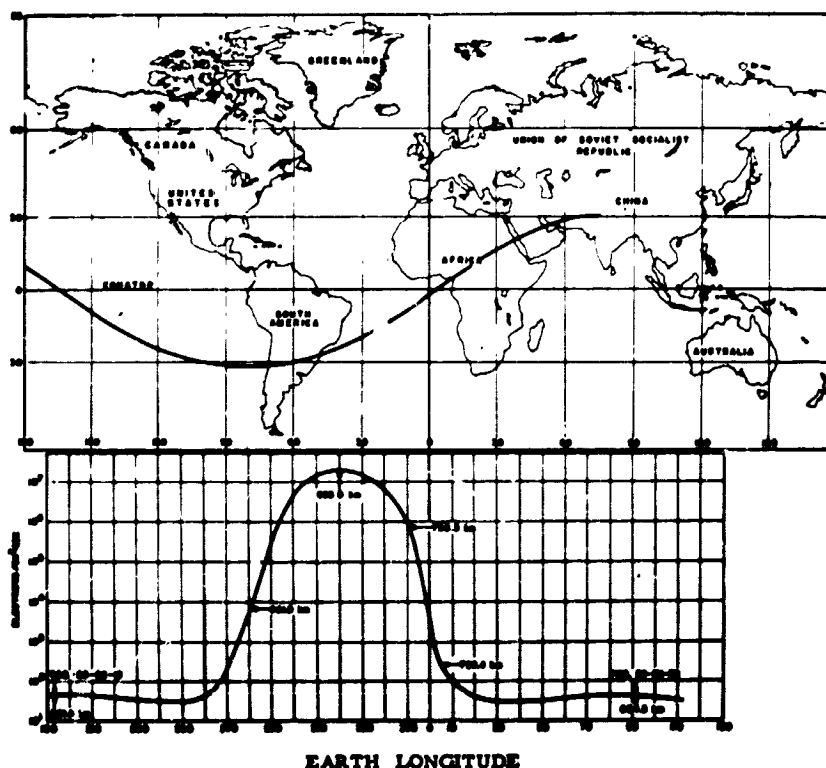


FIGURE 6. ELECTRON COUNT RATE FOR PATH THROUGH ANOMALY FOR PEGASUS I

The Pegasus radiation data are unique and extremely valuable due to the long lifetimes of the Pegasus satellites in this region. Before Pegasus data were obtained, the decay of the Starfish electrons was considered to be exponential. Based upon the analysis of Pegasus radiation data, a paper [8] was presented at the American Geophysical Union Meeting in April 1967 showing that:

(1) The decay of the 0.5-MeV electron flux at $L \lesssim 1.2$ deviated significantly from an exponential. The departure from the exponential was caused by a long-term flux enhancement, by a factor of as high as 4, from June 1965 to August 1965. This enhancement was related, but not clearly correlated to the magnetic activity. This effect was observed up to $L = 1.4$, but only at the higher B values.

(2) For $L > 1.5$, $B/B_0 \gtrsim 3$, the decay constant τ defined by $\phi = \phi_0 e^{-t/\tau}$, where ϕ is the omnidirectional flux for $E \gtrsim 0.5$ MeV, shows a strong B dependence. For example, at $L = 1.6$, $B/B_0 = 3$, $\tau = 194 \pm 16$ days, whereas at $B/B_0 = 3.3$, $\tau = 124 \pm 18$ days.

(3) The spectrum at $L > 1.5$ and high B/B_0 was found to harden with time during 1965.

(4) A change in the spatial distribution of the high-energy electrons was observed.

To extend and complete this study, B and L values will be examined closely, and temperature corrections will be made. While this is being done, the gross over-all radiation decay in the anomaly region as a whole will be examined. As a method of record-keeping, the peak fluxes for each day have been plotted. As the satellite orbit precesses and apogee occurs in the anomaly, the measured flux rises. The flux drops as the perigee enters the anomaly region. The period is approximately 18 days. Figure 7 shows the degradation of Pegasus I flux. Figure 8 indicates the degradation of Pegasus II flux. It is obvious that this information gives no indication as to the mechanism by which particles are removed from the belts, but only a method for estimating the decay.

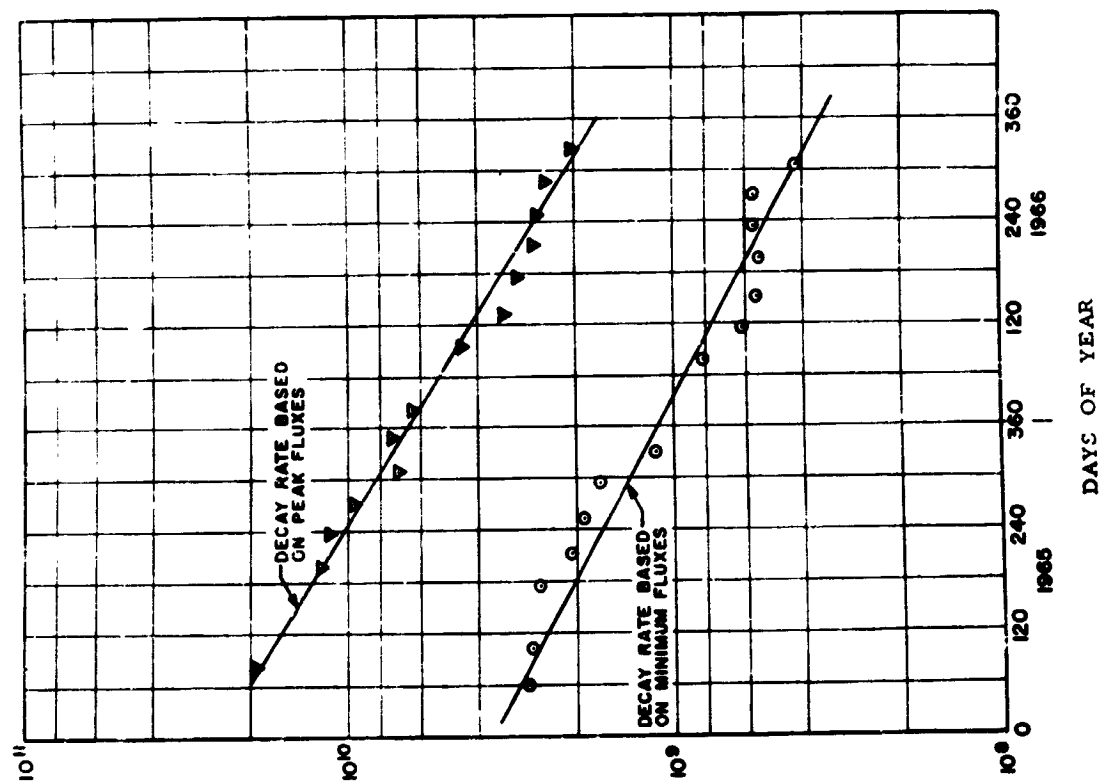


FIGURE 7. PEAK AND MINIMUM FLUXES VS. DAY OF THE YEAR FOR PEGASUS I

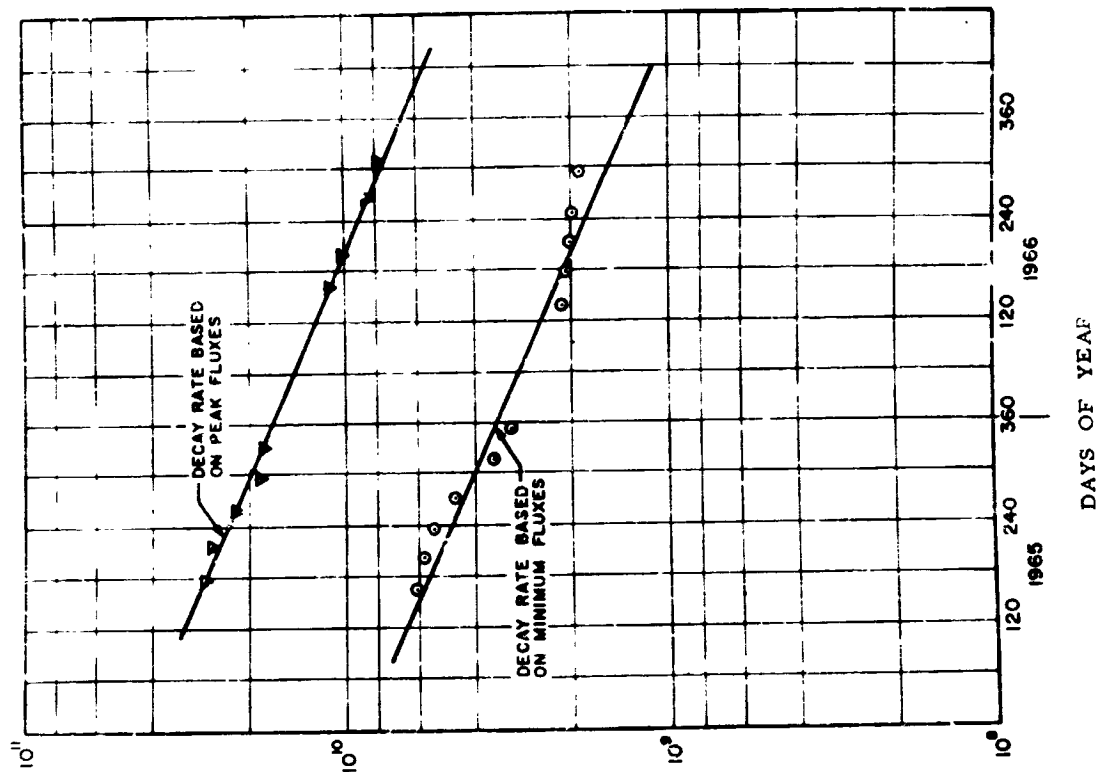


FIGURE 8. PEAK AND MINIMUM FLUXES VS. DAY OF THE YEAR FOR PEGASUS II

THERMAL MEASUREMENTS

There was a total of 24 'housekeeping' temperature probes on each Pegasus satellite, and five probes on a thermal control coatings experiment package. These probes provide the data used in making an evaluation of the thermal design of the spacecraft.

Degradation of the SMA S-13 White Coating

The service module adaptor (SMA) of each Pegasus satellite was coated with S-13 white coating (ZnO in methyl silicone, produced by the Illinois Institute of Technology Research Institute) to provide a large, low-temperature heat sink for the electronics package. Preflight calculations had estimated that the SMA average temperature should be about 220° K. This figure was based on predicted spacecraft motion and internal heat generation and on measured values of α_s/ξ_T (ratio of solar absorptance to total hemispherical emittance) for the S-13 coating. Actual flight temperatures for the SMA ran considerably higher than predicted on all three satellites. As is seen in Figures 9 and 10, the average temperatures for Pegasus I and III are on the order of 250° K, and this was also the case for Pegasus II. From the temperature and attitude data, in-flight values for α_s/ξ_T of the S-13 coating were calculated. The results shown in

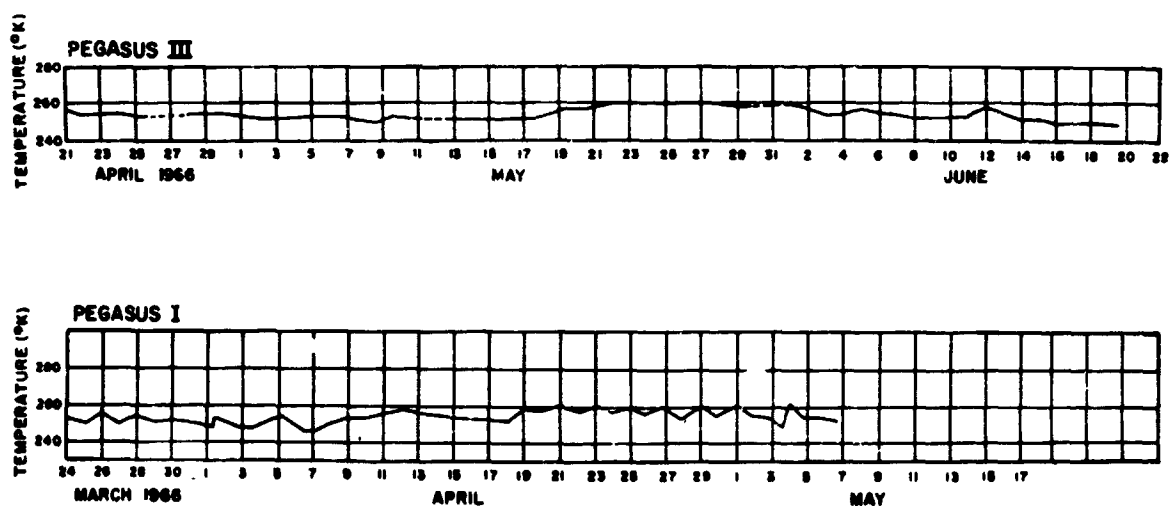


FIGURE 9. AVERAGE SMA TEMPERATURES FOR PEGASUS I AND III

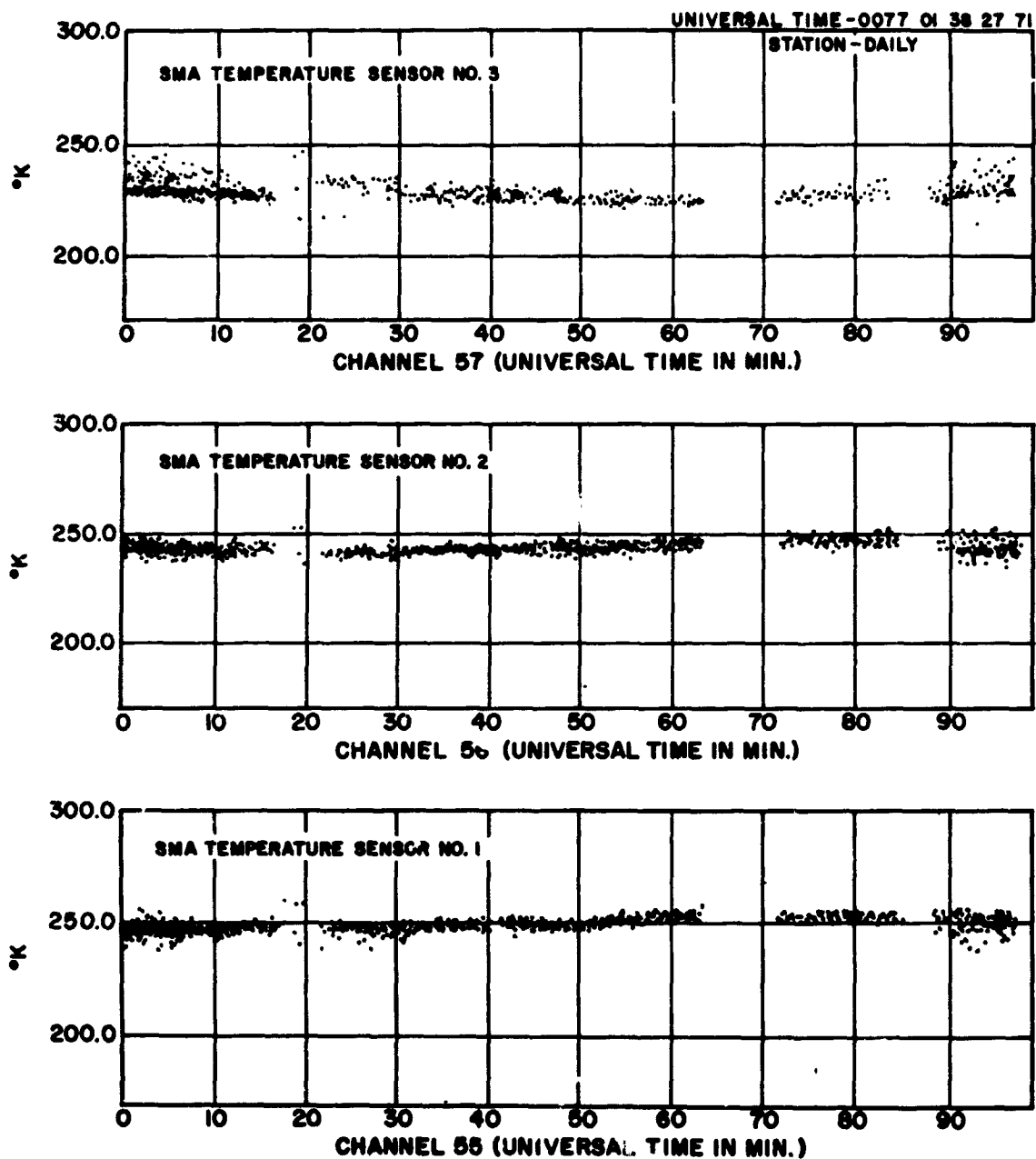


FIGURE 10. TEMPERATURE VS. TIME (PEGASUS I)

Figure 11 for Pegasus I were surprising in view of prelaunch measurements, but accounted for the high temperatures observed. As is seen in Figure 11, the value of α_s/ξ_T is on the order of 0.50, which is an increase of about 100 percent from prelaunch measurements. About 30 percent of this increase is accounted for by a vacuum effect which was later discovered. The cause or causes of the rest of the degradation have not been determined conclusively. Some of the possible factors are: (1) surface damage to the S-13 coating from LOX diffusion through the skin of the S-IV stage, (2) adsorption of vented hydrogen, and (3) retrorocket plume impingement. The possibilities of LOX damage and hydrogen adsorption were not investigated extensively because of the lack of data, but films of the S-IV separation were studied in detail. No visible darkening of the S-13 coating was evidenced, so the damage mechanism is still undetermined.

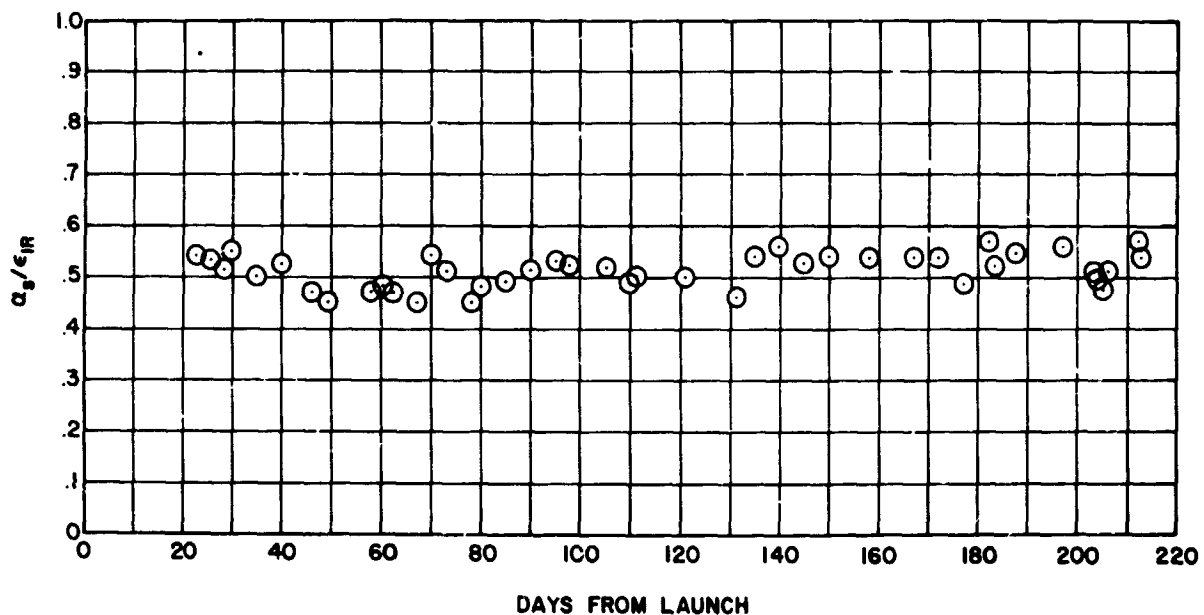


FIGURE 11. SMA α_s/ξ_T FOR S-13 COATING (PEGASUS I)

Louver Function

An active thermal control system in the form of louvers was mounted between the SMA radiative heat sink and the electronics canister. As was

previously stated, SMA temperatures ran 30° K to 40° K higher than expected due to degradation of the S-13 coating. The louver system served to compensate for the increased heatsink temperature by maintaining its blades at rather large opening angles most of the time. The opening angle was computed using SMA and electronics canister temperatures. This angle is shown plotted against time in Figure 12. The effectiveness of the louvers is illustrated in Table II which shows that the canister electronics were maintained at temperatures within the design limits. Figure 13 shows sample battery temperature data which fall well within design limits.

TABLE II. RANGE OF PEGASUS TEMPERATURES		
Component	Design Range (° K)	Actual Range (° K)
Pegasus I		
Radiation Detector	222 to 338	240 to 310
Batteries	272 to 322	295 to 300
Other Electronics	262 to 332	285 to 290
Solar Panels	194 to 339	215 to 320
Meteoroids Detect. Panels	167 to 394	215 to 370
Pegasus II		
Radiation Detector	222 to 388	240 to 310
Batteries	272 to 322	295 to 305
Other Electronics	262 to 332	285 to 325
Solar Panels	194 to 339	230 to 340
Meteoroid Detect. Panels	167 to 394	210 to 370
Pegasus III		
Radiation Detector	222 to 388	235 to 305
Batteries	272 to 322	295 to 314
Other Electronics	262 to 332	285 to 325
Solar Panels	194 to 339	235 to 310
Meteoroid Detect. Panels	167 to 394	220 to 350

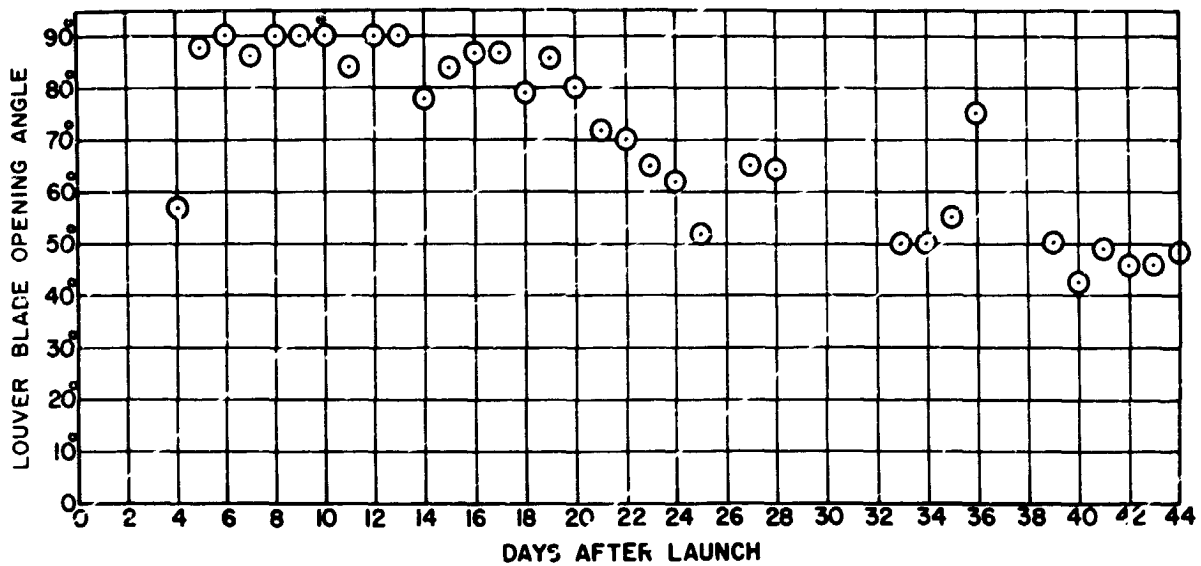


FIGURE 12. LOUVER BLADE OPENING ANGLE VS. TIME (PEGASUS I)

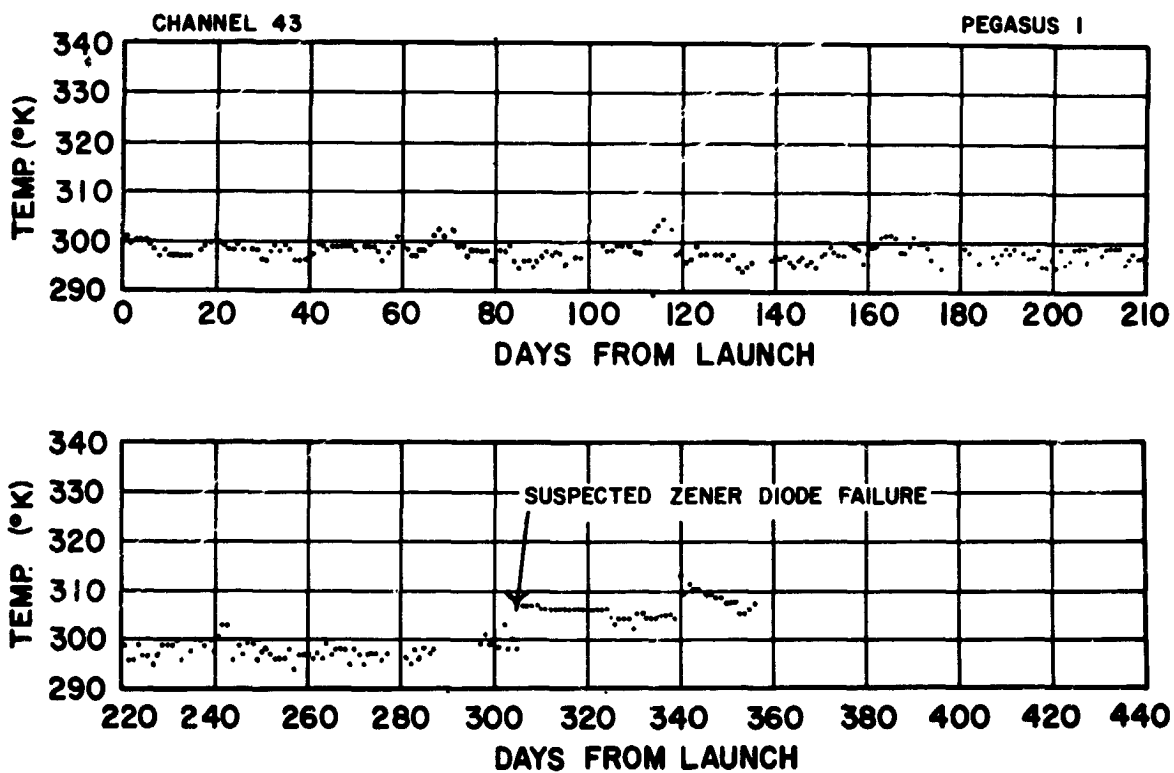


FIGURE 13. INTERNAL BATTERY TEMPERATURE (PEGASUS I)

The Micrometeoroid Detector Panels

The micrometeoroid detector panels on the Pegasus spacecraft were given an Alodine chemical conversion coating for thermal control surfaces. Each spacecraft had one dummy detector panel (15.24×15.24 cm) fitted with four thermocouples for monitoring temperatures and temperature gradients experienced as well as possible α_s/ξ_T degradation. Sample data from one of these temperature probes are shown in Figure 14. Using preflight values for the α_s and ξ_T of Alodine, theoretical temperature curves were calculated for the dummy panel and compared with actual flight data. One of these curves is shown in Figure 15 for Pegasus I about two months after launch. It may be seen from this that there was no apparent α_s/ξ_T degradation of the Alodine at that time. Similar data through November 1965 for Pegasus I indicate very little degradation.

Thermal Control Coating Degradation Experiment

Each Pegasus spacecraft carried a thermal control coatings experiment package containing four coating samples as follows:

<u>Pegasus I</u>	<u>Pegasus II</u>	<u>Pegasus III</u>
Lowe Bros. Black	Lowe Bros. Black	Lowe Bros. Black
S-13	S-13	S-13
Alodine	Alodine	Alodine
Rutile	Z-93	Z-93

The blackcoated sensors were used as references for the calculation of α_s/ξ_T values for the others. Sample sensor temperature data are shown in Figure 16. The α_s/ξ_T values calculated from Pegasus I data are shown in Figure 17. It may be seen that the S-13 coating experienced an almost instantaneous degradation of about 30 percent. This resulted from a vacuum effect that was not expected before launch, since at that time all of the laboratory α_s measurements had been made in air. Similar data from Pegasus II are shown in Figure 18. It may be seen in both cases that degradation of the S-13 coating appears to have leveled off at an α_s/ξ_T value of about 0.40. Alodine appears

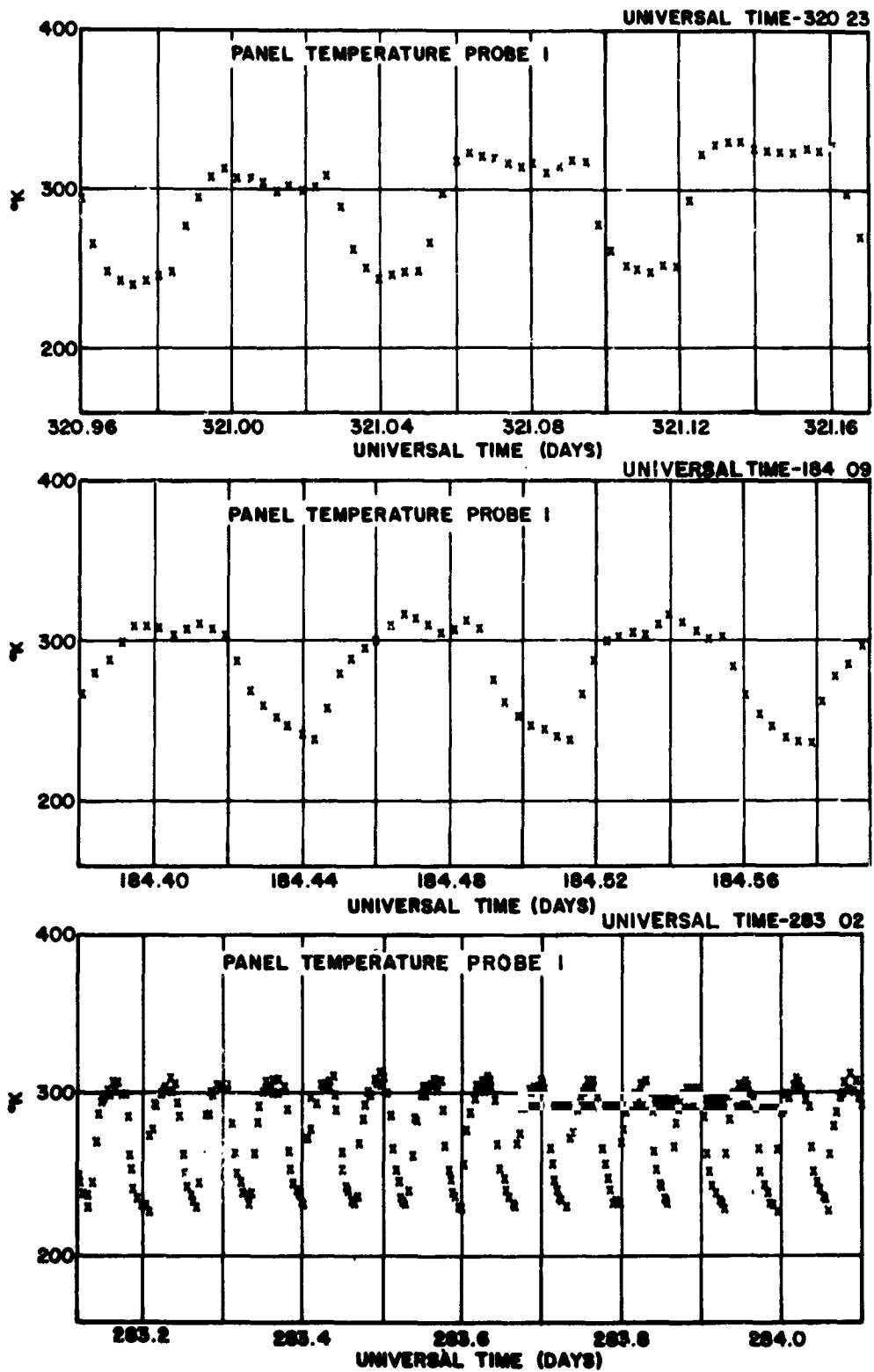


FIGURE 14. DETECTOR PANEL TEMPERATURE VS. TIME (PEGASUS I)

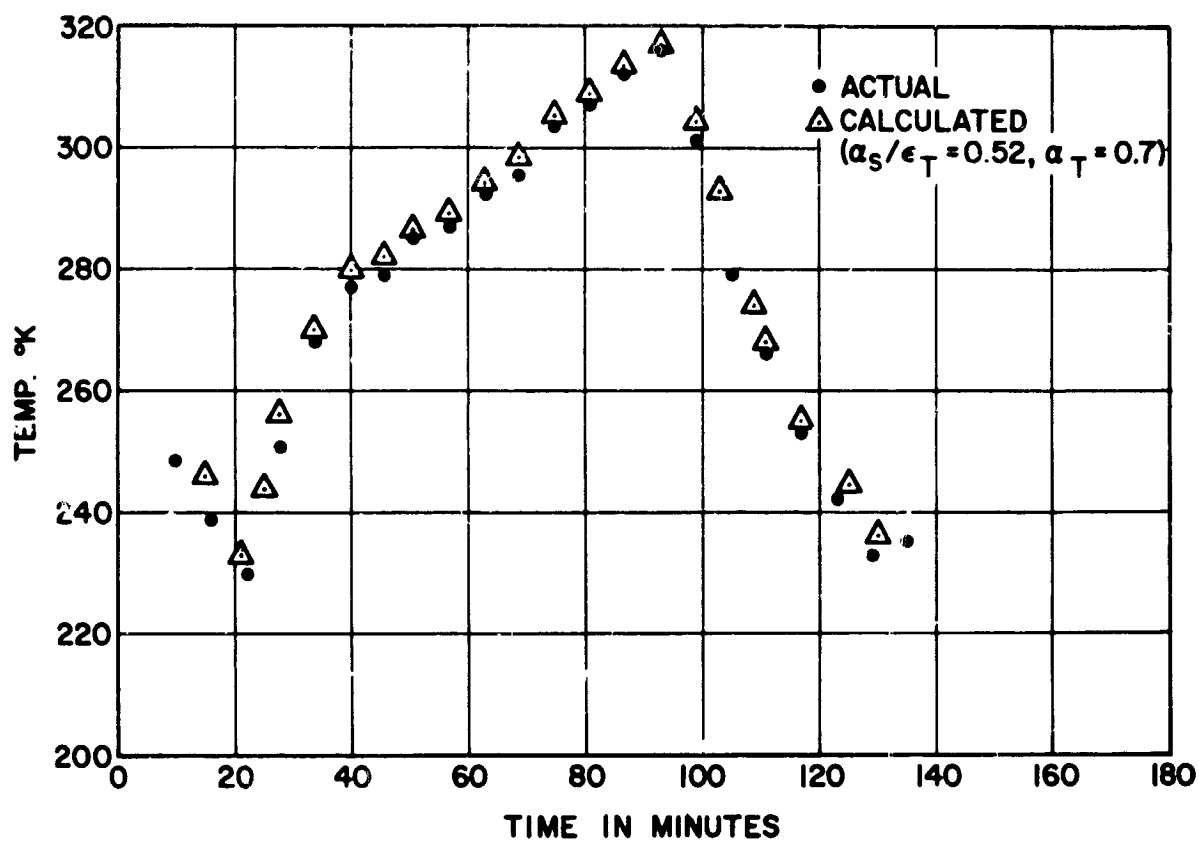


FIGURE 15. ACTUAL AND CALCULATED PANEL TEMPERATURE (PEGASUS I)

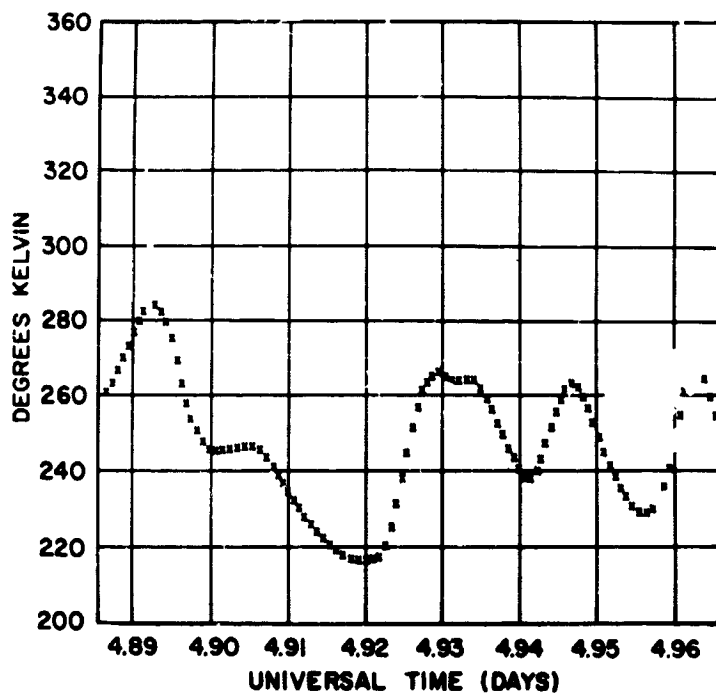


FIGURE 16. Z-93 COATING TEMPERATURE VS. TIME (PEGASUS II)

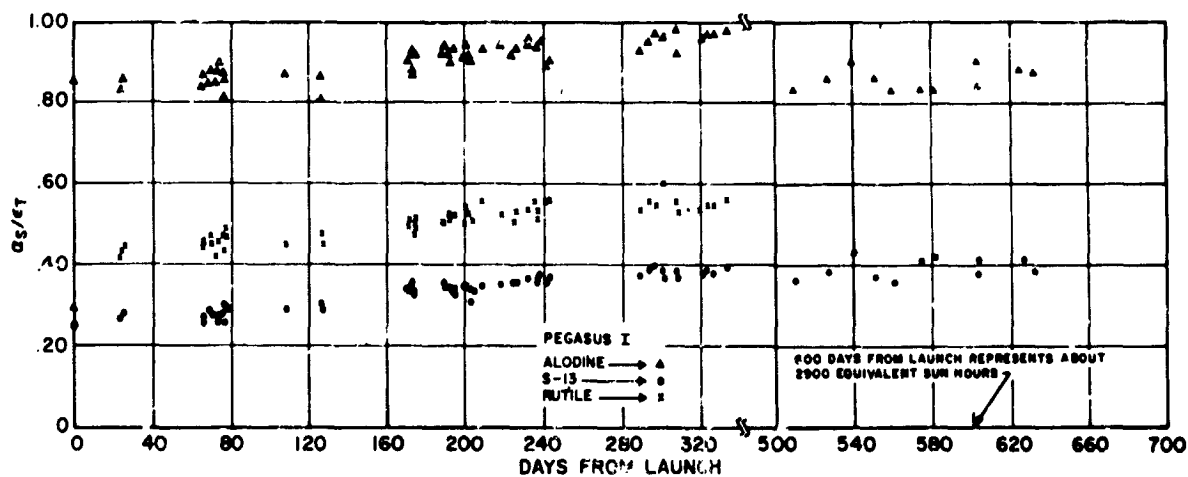


FIGURE 17. α_s/ϵ_T VALUES VS. TIME (PEGASUS I)

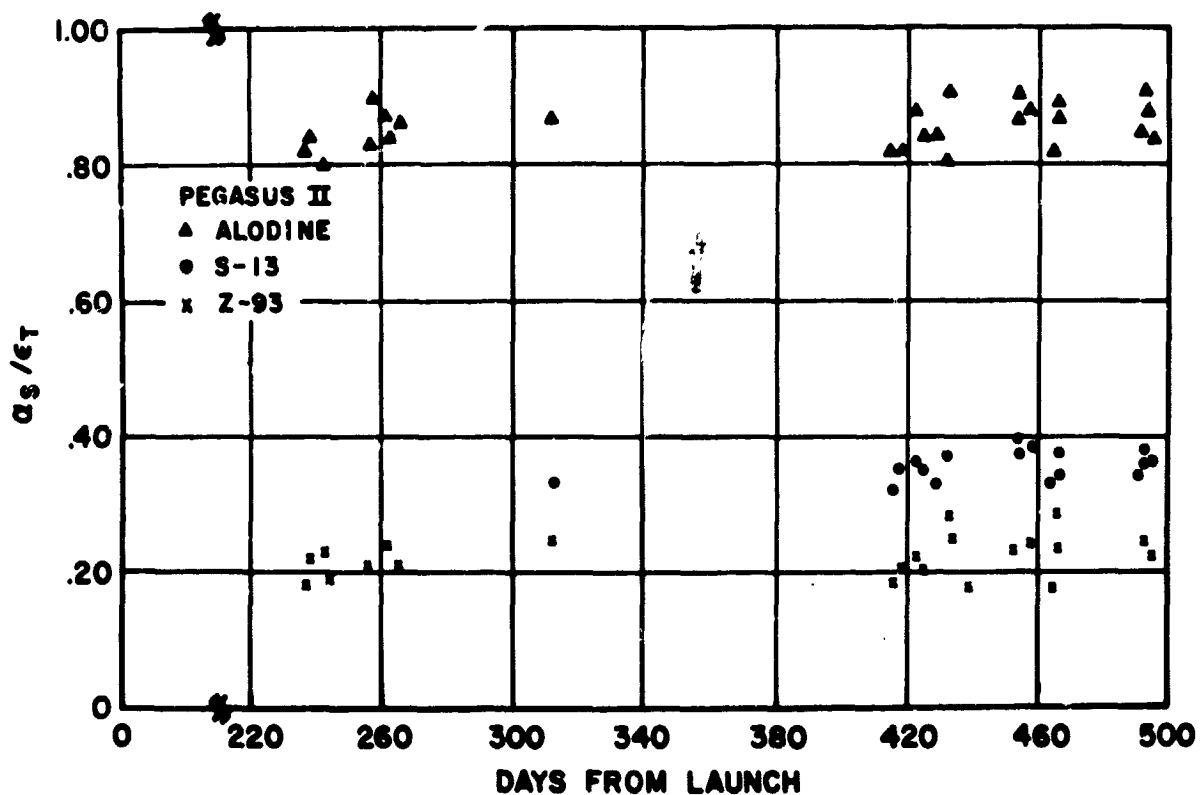


FIGURE 18. α_s/ϵ_T VALUES VS. TIME (PEGASUS II)

to have come to a final state with an α_s/ξ_T value approximately equal to the prelaunch value of 0.86. The Rutile, a known degradable, appears to have leveled off at about 0.55 to 0.60. The Z-93 coating (ZnO in potassium silicate) which is also used on the Apollo capsule, appears to have undergone no appreciable degradation.

The "Heat-of-Fusion" Sensor

The reference sensor (coated with Lowe Bros. black paint) in the Pegasus III thermal control coatings experiment package consisted of a hollow cylinder containing a small amount of the paraffine, hexadecane. This material melts at about 293°K and has a high heat of fusion. Its presence serves to damp thermal oscillations of the sensor, as shown in Figure 19. This concept for passive thermal control of spacecraft is now under extensive investigation.

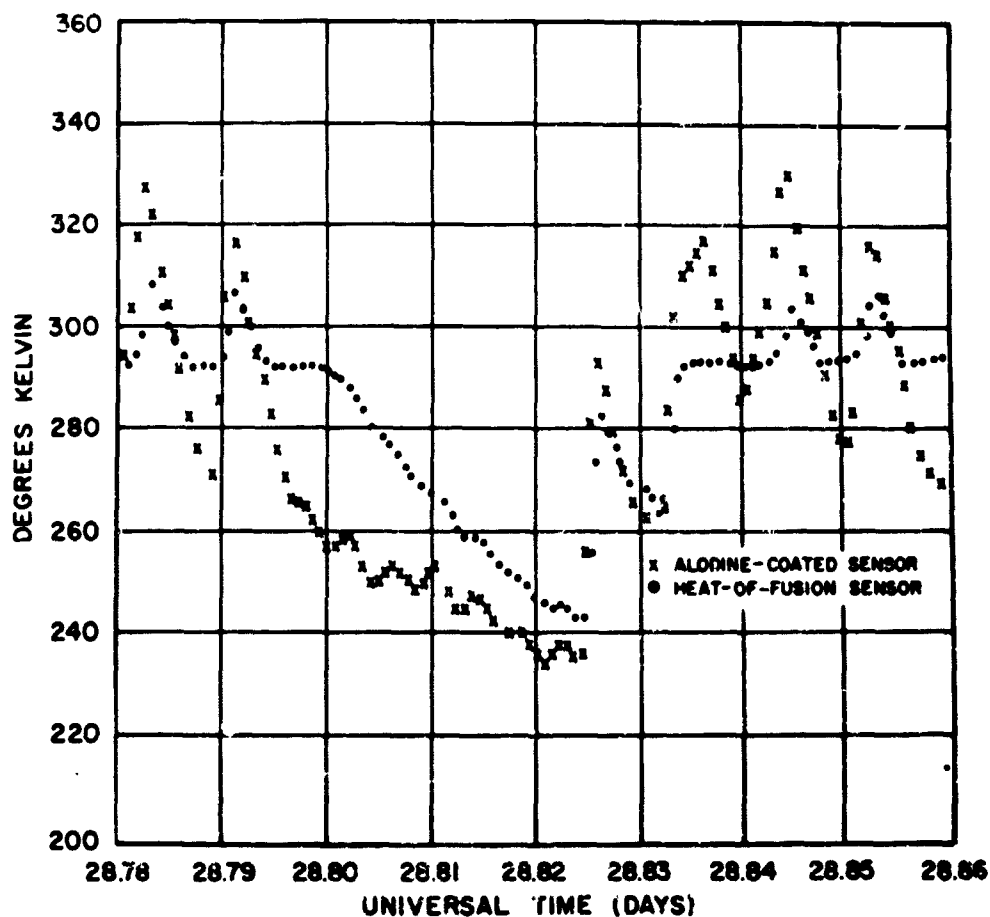


FIGURE 19. DAMPING OF TEMPERATURE OSCILLATIONS IN HEAT-OF-FUSION SENSOR COMPARED TO ALODINE SENSOR (PEGASUS III)

EARTH ALBEDO MEASUREMENTS*

The temperature data from the thermal control coatings experiment package provided a convenient source of input for calculations of the earth's albedo. Equations describing thermodynamic equilibrium of two of the thermal sensors were solved simultaneously for the earth albedo term, defined in this case as the ratio of reflected to incident solar radiant flux. Earth infrared contribution was eliminated by the choice of proper sensors. The thermal input consisted of simultaneous data from the black reference coating sensor and the white S-13 coating sensor.

Resulting values of earth albedo obtained by this procedure were plotted as a function of the corresponding earth longitude. Three such curves are shown in Figures 20, 21, and 22; the orientation of the Pegasus spacecraft was a limiting factor in the availability of usable thermal input data, and thus the temporal separation of the albedo data is rather large. However, these curves correspond to widely separated geographic regions and cover a large variety of topographical features with which to establish some correlation.

Coupled with the analysis of these results, certain nephanalyses (cloud charts) and photographs from Tiros IX were studied to establish a correlation of earth cloud cover with earth albedo. The results are presented as sections of the pertinent nephanalyses with the projected orbit of Pegasus I plotted for reference.

In Figure 23, the first albedo curve is plotted directly under the corresponding Tiros cloud chart. A smooth curve drawn through the data points, ignoring the large central peak, would approximate the curve predicted by assuming the earth to be a diffuse reflector and postulating Rayleigh scattering of incident sunlight in the atmosphere. As Pegasus progressed in its orbit, the sensor normal pointed through progressively deeper layers of the earth's atmosphere so that Rayleigh scattering would, indeed, have become increasingly more prominent in providing sensor heat input and, thus, in determining the shape of the calculated albedo curve.

* The general source of information for this section is "Earth Albedo Studies Using Pegasus Thermal Data" by R. C. Linton; AIAA Thermophysics Specialists Conference, no. 67-332, New Orleans, La., April 17-20, 1967.

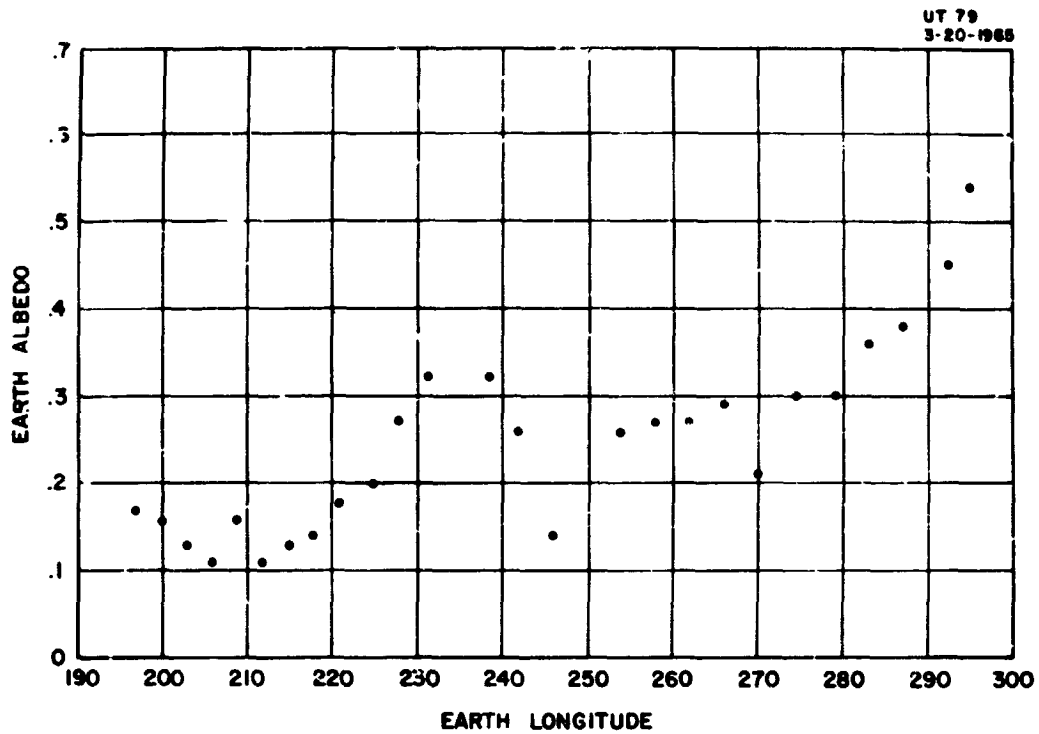


FIGURE 20. EARTH ALBEDO FROM PEGASUS I THERMAL DATA.
MARCH 20, 1965.

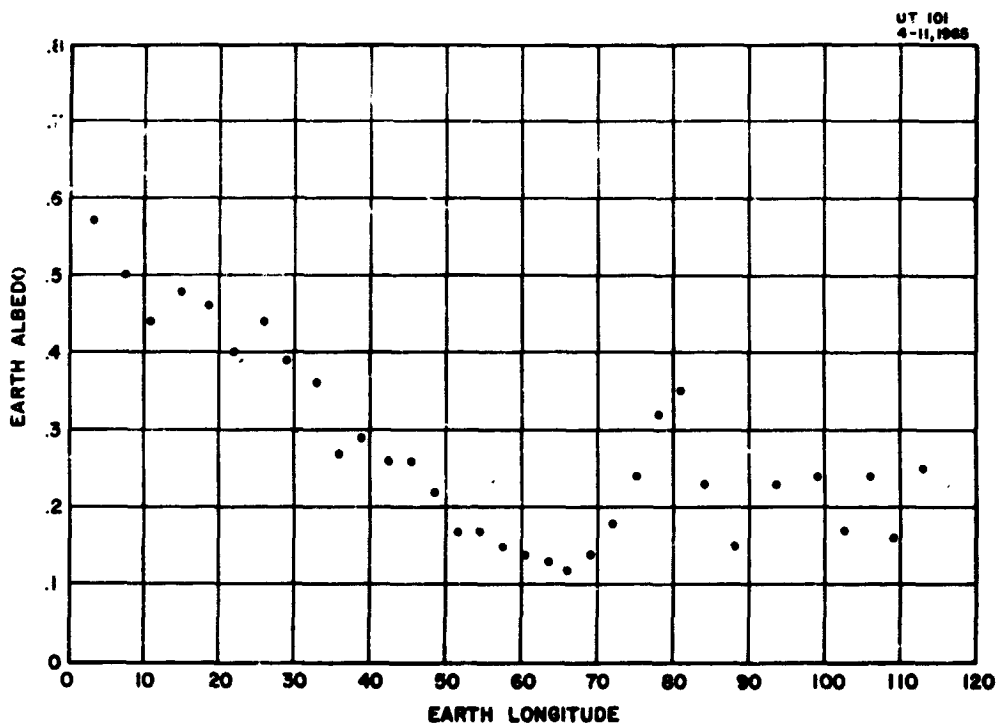


FIGURE 21. EARTH ALBEDO FROM PEGASUS I THERMAL DATA.
APRIL 11, 1965

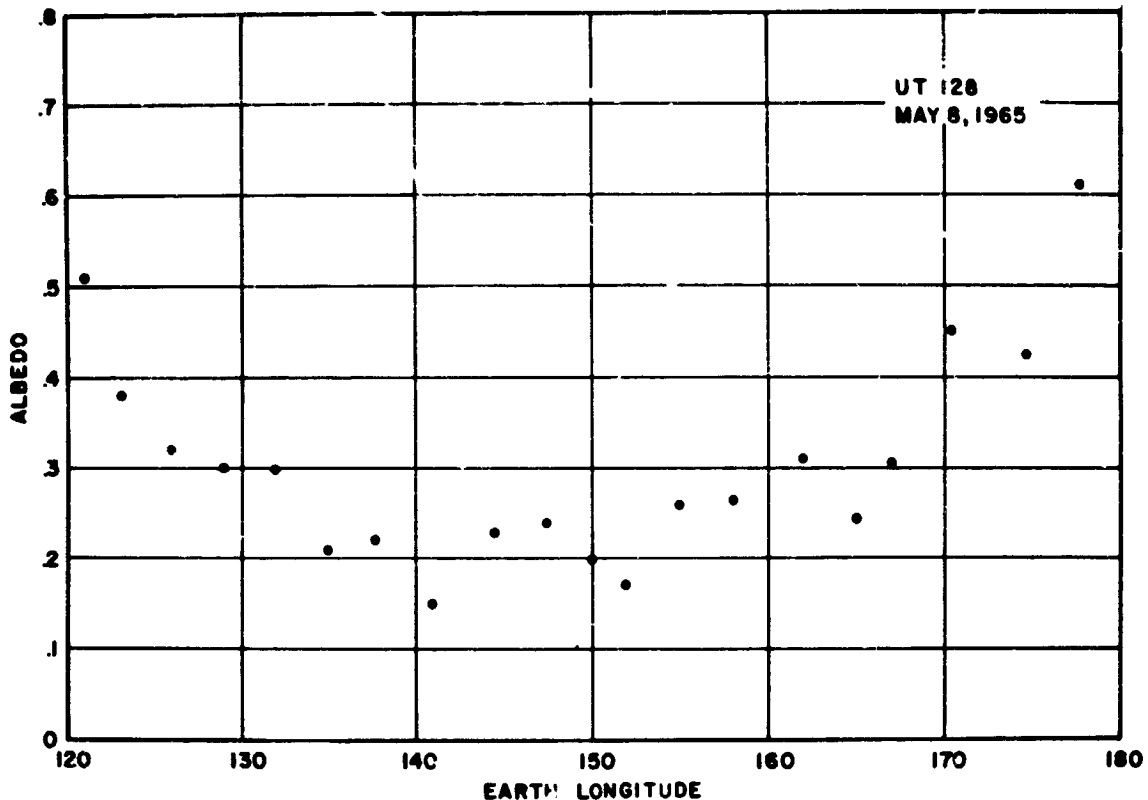
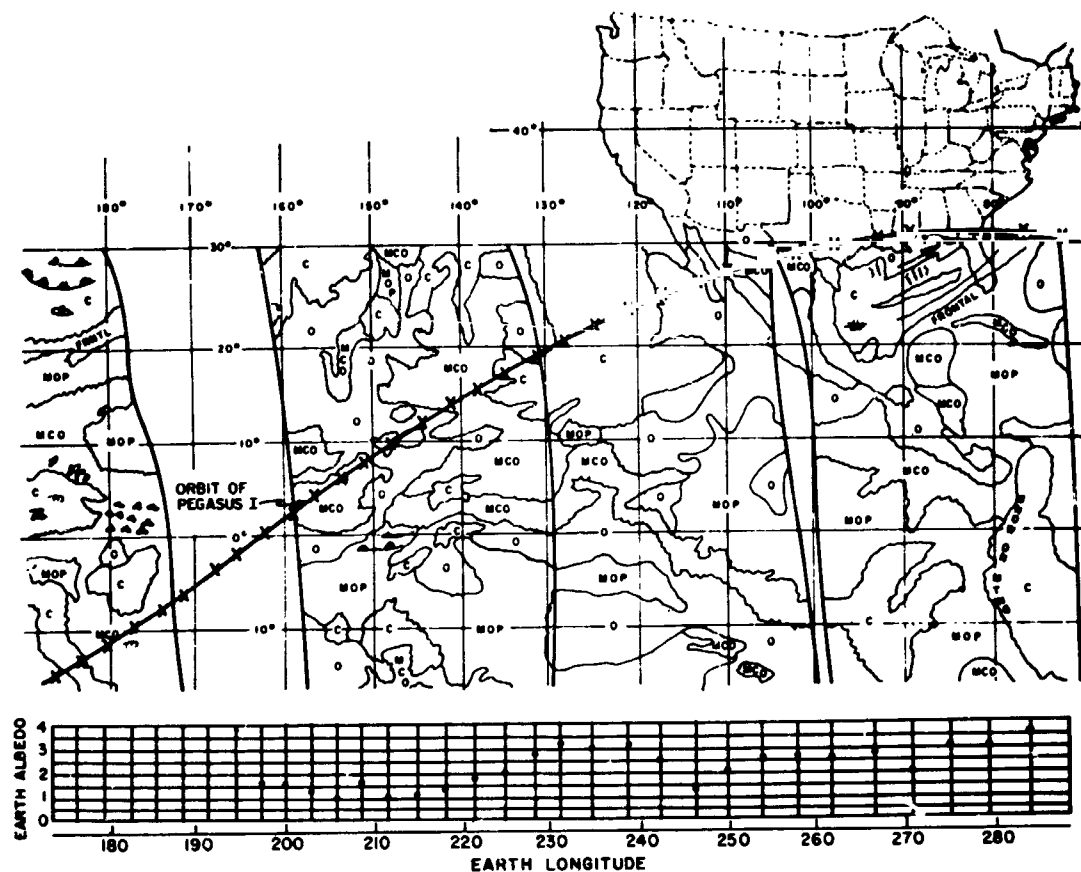


FIGURE 22. EARTH ALBEDO FROM PEGASUS I THERMAL DATA.
MAY 8, 1965.

As shown in Figure 23, the dominant feature of the area viewed by the Pegasus sensor is the extensive cloud cover. The central peak observed in the albedo curve should correspond to the great cloud mass lying southwest of the North American coastland. East of this great cloud mass, a large open area is shown which should account for the rapid decrease in albedo values corresponding to this region. Not shown in Figure 23, but readily observed in the Tiros IX photographs, is a region of highly varied cloud coverage lying north of 30° latitude. The distribution of this cloud cover precludes a precise correlation with the albedo values, although the overall density is sufficiently high to produce the albedo magnitudes shown through 270° longitude. The remainder of the albedo curve, as previously mentioned, could result from Rayleigh and Mie scattering in the earth's atmosphere. A more illustrative, though less accurate, presentation of these data is given in Figure 24.

Pegasus I thermal data, received on April 11, 1965 (Fig. 21), were used in obtaining the albedo results discussed in this paragraph and the two that follow. As can be seen in Figure 25, the first half of the projected orbit of



NOTE SEE FIGURE 24 FOR KEY TO CLOUD COVERAGE SYMBOLS.

**FIGURE 23. CALCULATED EARTH ALBEDO CORRELATED WITH
TIROS IX CLOUD CHART, USING PEGASUS I THERMAL DATA.
MARCH 20, 1965.**

Pegasus crosses the northern regions of Africa; and almost total lack of cloud cover over this area on April 11, 1965 provided an opportunity to observe the unperturbed albedo of the underlying surface.

Magnitudes of initial points of this albedo curve may be explained by postulating Payleigh and Mie scattering in the atmosphere and considering the high reflectivity of desert sands such as those the projected orbit crosses. As the satellite moved over the surface, the sensor normal intersected progressively less of the earth's atmosphere, thus decreasing the importance of Rayleigh scattering in the albedo received by the Pegasus sensors (the negative slope of the albedo curve). The curve through longitude 40 reflects this decrease.

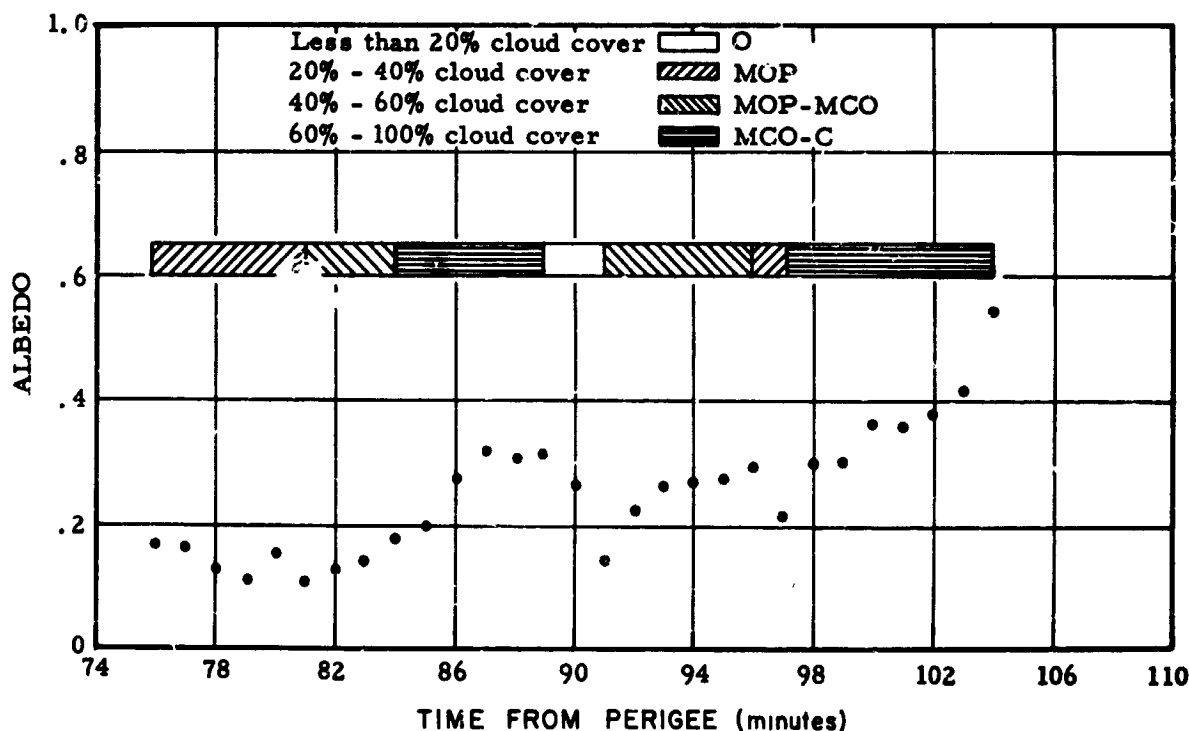


FIGURE 24. CORRELATION BETWEEN ALBEDO AND CLOUD DENSITY - PEGASUS I. MARCH 20, 1965.

The surface contributing to the remaining portion of the albedo curve consists mainly of ocean waters. A decreasing slope with relatively small magnitudes of albedo between 40° and 70° longitude (Fig. 25) should correspond to the low reflectivity of these ocean waters. Although scattered cloud cover over this area was observed in Tiros IX nephanalyses for this date, it was not significant. Predominant cloud masses, however, were centered about the area corresponding to the large peak in the albedo curve at longitude 80, and this is a striking illustration of the effect of massive cloud formations. The remaining points of this albedo curve, all of which are not shown, are relatively scattered due in part to the variable distribution of cloud cover over the corresponding surface.

Figure 22 shows the results of the thermal data received from Pegasus I on May 8, 1965. A smooth curve drawn through the data points would closely approximate the shape predicted by an assumption of diffuse reflection on the

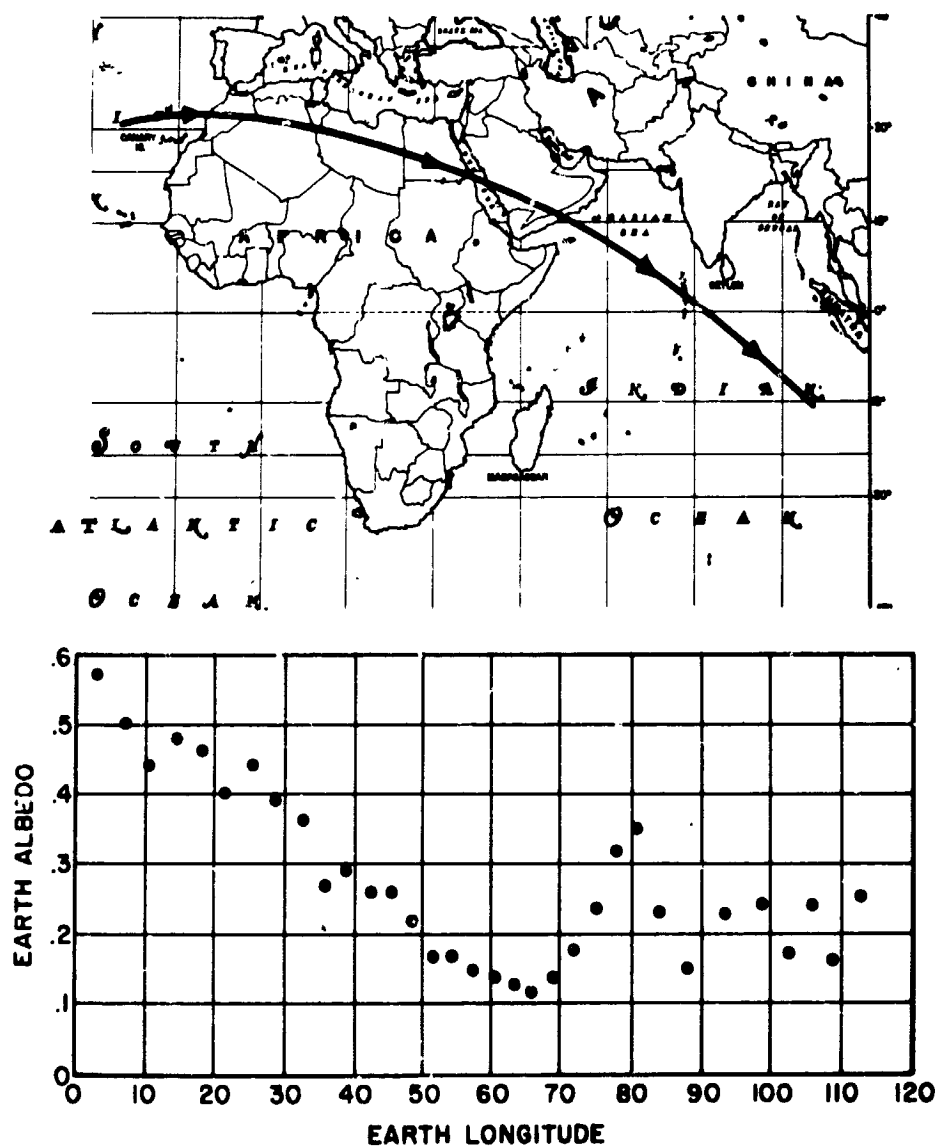


FIGURE 25. PROJECTED ORBIT OF PEGASUS I WITH CALCULATED ALBEDO. April 11, 1965

earth's surface and Rayleigh scattering in the atmosphere. The projected orbit of Pegasus for this case, beginning at 120° longitude, passes the northern coastline of Australia and continues over the Coral Sea to the Mid-Pacific region. Thus, for the greater part of this orbit, the Pegasus sensors were receiving albedo from ocean surfaces. Tiros IX meteorological data are of little significance for interpreting this albedo curve, not only because of a relatively scarcity of photographic coverage but because of the mixed density of

cloud coverage. The uniformity of surface characteristics and lack of dominating cloud masses apparent from a study of the Tiros IX photographs should, however, explain the lack of a large peak in the albedo curve.

These results illustrate the variety and usefulness of Pegasus thermal data as a source of input to studies of the earth's thermal environment.

ROTATIONAL MOTION OF PEGASUS SATELLITES

The attitude sensing system and attitude data reduction methods for Pegasus have been reported elsewhere [1]. This section is merely a summary of the more significant results observed from the orientation data derived for the three Pegasus spacecraft.

The first unexpected observation was the initial spin of 10 deg/sec (max) on Pegasus I. Shortly after injection into orbit the spacecraft began to spin about its longitudinal axis. The cause of this spin was attributed to the venting of residual gases from the S-IV stage. Changes in the venting lines on the subsequent flights of Pegasus II and III reduced the initial spin to 6 1/2 deg/sec (max) for these two spacecraft.

The next unusual observation was the short period fluctuations, which resembled nutations, in the sun aspect curves. Subsequent analyses proved that these fluctuations were caused by refraction of the sunlight through the quartz sun sensor blocks. After proper correction was made to the calibration curves for the sun sensors, the fluctuations were eliminated.

Another phenomenon, yet unexplained, was the differences observed in the precession time histories for the three satellites. After the spin on Pegasus I reached the 10 deg/sec maximum about its least moment of inertia axis, it began to precess in a conical fashion. The half cone angle of precession continued to increase until it reached the 90° "flat tumble" mode after 14 days. The spin was then stabilized about the maximum moment of inertia axis. Pegasus II did not undergo this transition, and it took Pegasus III almost a full year to make the transition from a spin about the minimum moment of inertia axis to a spin about the maximum moment of inertia axis.

Another significant event was the decay of the spin motion of the spacecraft. The spin decayed rather steadily on all three Pegasus satellites. This was attributed to the effects of magnetic eddy currents.

The most significant observation from the analysis of the orientation data and theoretical analysis was the long term periodic motion of the spin axis. Figure 26 shows this periodicity. The angles θ and ϕ are the spherical

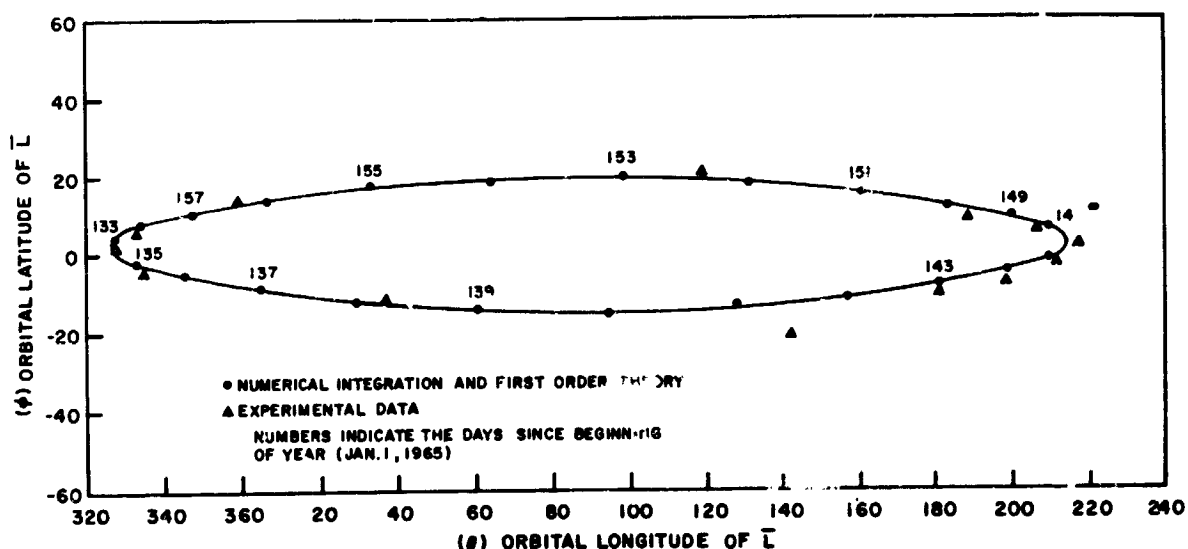


FIGURE 26. ANGULAR MOMENTUM VECTOR MOTION - PEGASUS I SATELLITE

coordinate angles which define the position of the angular momentum vector which coincides with the spin angular velocity vector if there is no nutation angle. The angles are referred to a moving coordinate system which is defined by the line of nodes and the orbital angular momentum vector. The theoretical development which predicts this long-term motion is given in the next section of this report, "Rigid Body Rotational Theory."

This theory is applicable to rotating bodies. Therefore, when the spin of the Pegasus satellites decayed to a rate on the order of the orbital rate, the spacecraft began librating. All three Pegasus satellites are presently in this mode. This is a very difficult problem to correlate theoretically and experimentally since the observational uncertainty in a full three-axis orientation is approximately 20° due to the inherent inability of the infrared earth sensors to define the vector to the center of the earth.

RIGID BODY ROTATIONAL THEORY

The observations of the orientation of the Pegasus Satellites, which were telemetered from onboard sun and earth sensors, motivated extensive research on analytical methods for describing the rotational motion of orbiting triaxial rigid bodies. The result of this research has been the development of a new first-order theory for the rotational motion of triaxial satellites. Three integrals were derived, by the averaging principle of Kryloff and Bogoliuboff, which determine the motion of the rotational angular momentum vector. The results are applicable to natural or artificial orbiting bodies. This section briefly describes this new method.

The gravitational equation of motion for the angular momentum vector of a small triaxial orbiting rigid body with respect to the (x, y, z) rotating orbit plane coordinate system (Fig. 27) may be written [9]

$$\frac{d\vec{L}}{dt} = \frac{3MG}{R^5} \vec{R} \times (I) \vec{R} - \vec{\Omega} \times \vec{L}. \quad (1)$$

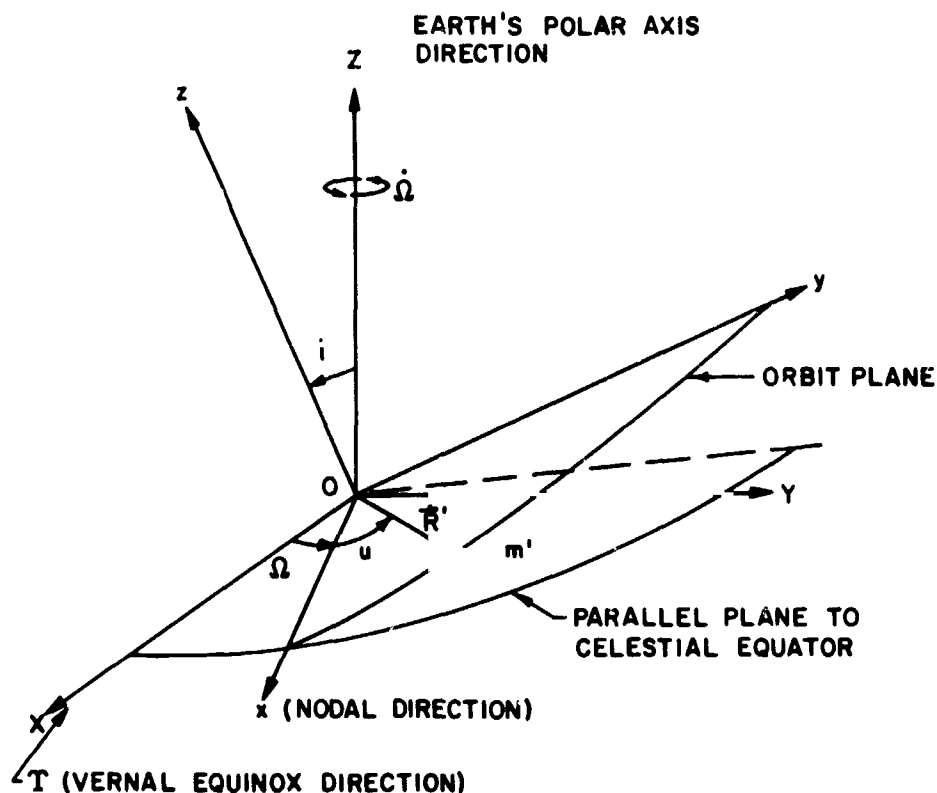
The vector \vec{L} is the angular momentum vector of the small body, MG is the gravitational constant of the primary, \vec{R} is the vector from the center of mass of the small body to the center of mass of the primary, (I) is the moment of inertial matrix of the small body with respect to the rotating coordinates and $\vec{\Omega}$ is the angular velocity vector of the rotating (x, y, z) coordinates due to possible regression of the orbit plane.

The matrix (I) may be written as

$$(I) = (T) (I') (T)^T \quad (2)$$

where (T) is the transformation from the principal axes of the small body to the rotating orbit plane coordinates and $(I)'$ is the diagonalized principle moment of inertial matrix.

$$(I)' = \begin{pmatrix} I_1' & 0 & 0 \\ 0 & I_2' & 0 \\ 0 & 0 & I_3' \end{pmatrix}.$$



(O,X,Y,Z)- ARE CONSIDERED PARALLEL TO INERTIAL COORDINATES
O IS THE PRIMARY m CENTER OF MASS

(O,x,y,z)- ARE THE ROTATING ORBIT PLANE COORDINATES

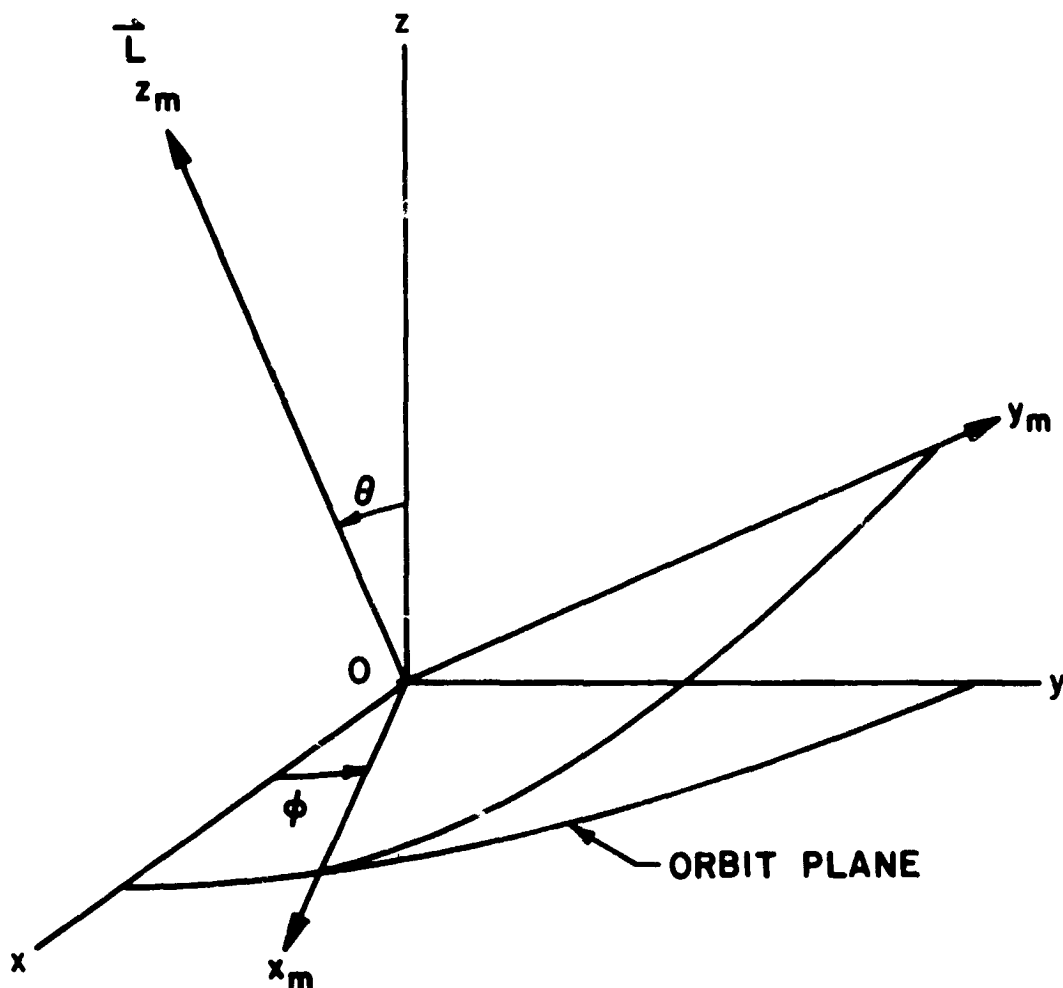
FIGURE 27. GEOMETRY OF THE ROTATING ORBIT PLANE
COORDINATE SYSTEM

Now (T) is to be written as the product of two matrices (M) and (B)

$$(T) = (M) (B) \quad (3)$$

where (M) is the transformation matrix from angular momentum vector coordinate system to the rotating orbit plane system (see Fig. 28), and (B) is the transformation from the principal axes of the small body to the angular momentum coordinate system (see Fig. 29).

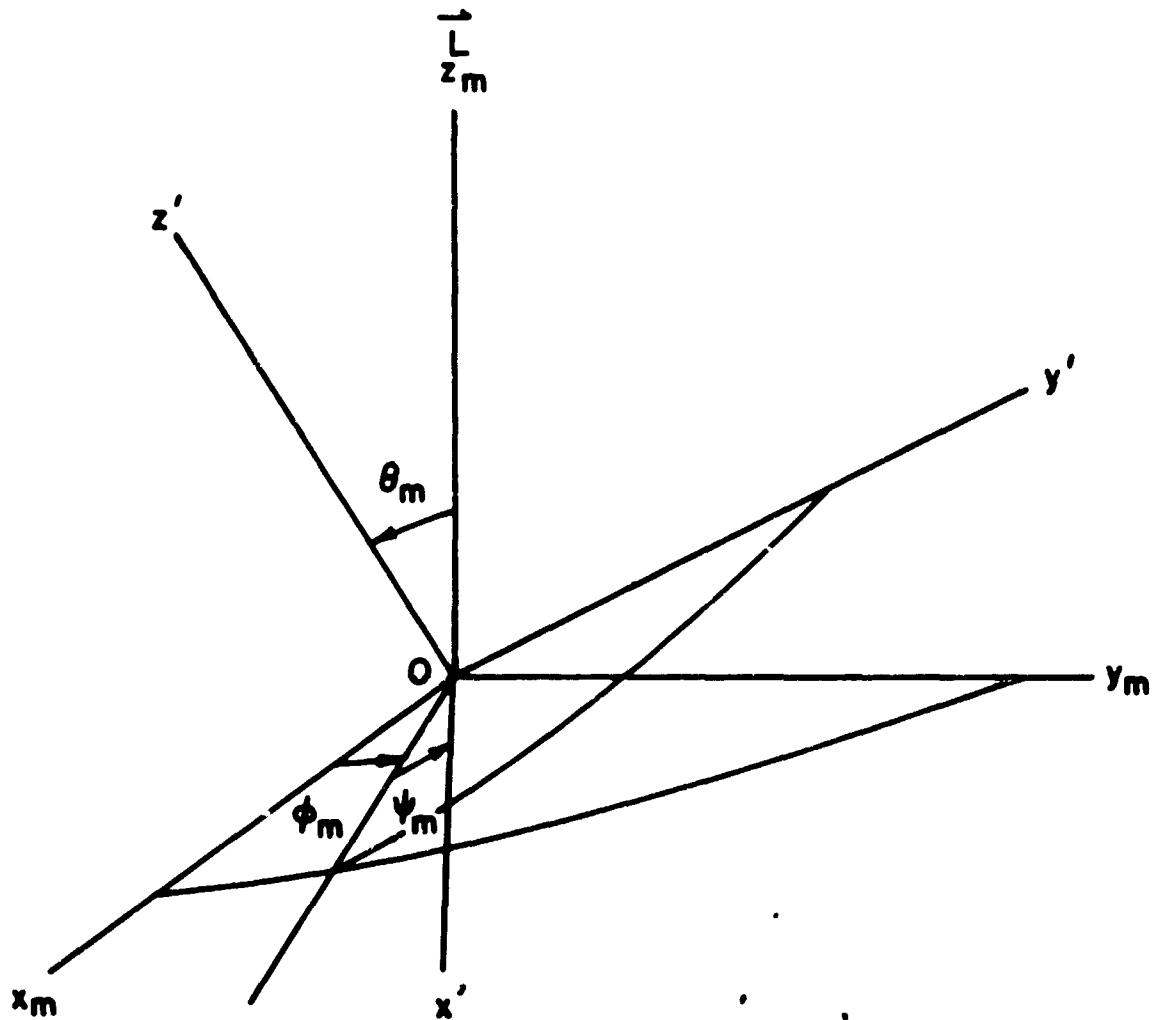
Note that the elements of (M) are functions of θ and ϕ which define the position of \vec{L} . The elements of (B) are functions of θ_m , ϕ_m , and ψ_m which



(O, x, y, z) ARE SAME AS DEFINED IN FIGURE 27

(O, x_m, y_m, z_m) ARE COORDINATES DEFINED WITH z_m ALONG THE \vec{L} VECTOR. THIS IS REFERRED TO AS THE MOMENTUM COORDINATE SYSTEM.

FIGURE 28. GEOMETRY OF THE ANGULAR MOMENTUM VECTOR COORDINATE SYSTEM



(O, x_m, y_m, z_m) ARE SAME AS DEFINED IN FIGURE 28

(O, x', y', z') ARE THE RIGID BODY COORDINATES ALONG
THE PRINCIPLE MOMENT OF INERTIA AXES

FIGURE 29. GEOMETRY OF THE PRINCIPAL AXES
COORDINATE SYSTEM

define the nutation, precession and spin angles of the small body with respect to the angular momentum coordinate system. The angular momentum system would remain fixed if there was no torque on the small body.

From Figure 27 it can be seen that

$$\dot{\vec{\Omega}} = \begin{pmatrix} 0 \\ \dot{\Omega} \sin i \\ \dot{\Omega} \cos i \end{pmatrix} \equiv \begin{pmatrix} 0 \\ -A \\ -B \end{pmatrix} \quad (4)$$

and

$$\vec{R} = \begin{pmatrix} R \cos u \\ R \sin u \\ 0 \end{pmatrix} \quad (5)$$

where i is the inclination of the orbit plane, $\dot{\Omega}$ is the regression rate of the line of nodes and u is the argument of latitude of the small body.

Combining all of the above equations with equation (1) gives

$$\frac{d\vec{L}}{dt} = \frac{3MG}{R^5} \vec{R} \times (M) (B) (I)' (B)^T (M)^T \vec{R} - \dot{\vec{\Omega}} \times \vec{L}. \quad (6)$$

If the rotational kinetic energy is large compared to the gravitational potential energy, then the averaging principle of Kryloff and Bogoliuboff may be applied to equation (6). Performing this average over a cycle of u , ϕ_m and

ψ_m gives

$$\frac{d\vec{L}}{dt} = \frac{K}{L^2} \left(\hat{\Omega} \cdot \vec{L} \right) \vec{\Omega} \times \vec{L} - \dot{\vec{\Omega}} \times \vec{L}. \quad (7)$$

where

$$K = - \frac{3MG}{8R^5} (I_1' + I_2' - 2I_3') (1 - 3 \cos^2 \phi_m).$$

A first integral of equation (7) is

$$L_x^2 + L_y^2 + L_z^2 = C_1 \text{ (A constant).} \quad (8)$$

A second integral is

$$L_y = \frac{K}{2AL^2} L_z^2 - \frac{B}{A} L_z + C_2 \quad (9)$$

where C_2 is a constant

$$\text{and } -At + C_3 = \int \frac{dl_z}{\sqrt{C_1 - \left(\frac{K}{2AL^2} L_z^2 - \frac{B}{A} L_z + C_2 \right)^2 - L_z^2}}. \quad (10)$$

The first integral states that the motion of the end point of \vec{L} takes place on the surface of a sphere. The second integral states that the motion takes place on the surface of a parabolic cylinder; therefore, the motion takes place on the path formed by the intersection of a parabolic cylinder with a sphere. The third elliptic integral in equation (10) implies that the motion is periodic.

Figure 30 is a plot of the normalized components of \vec{L} , in the y, z plane, which were calculated from the second integral given by equation (9), data from the Pegasus I satellite, and numerical integrations.

Figure 31 is a conceptual sketch of possible paths of motion. The particular path which the angular momentum vector takes up depends on the physical characteristics of the small body and its initial conditions. It may be of practical astronomical significance to note that both of these conditions may be controlled passively.

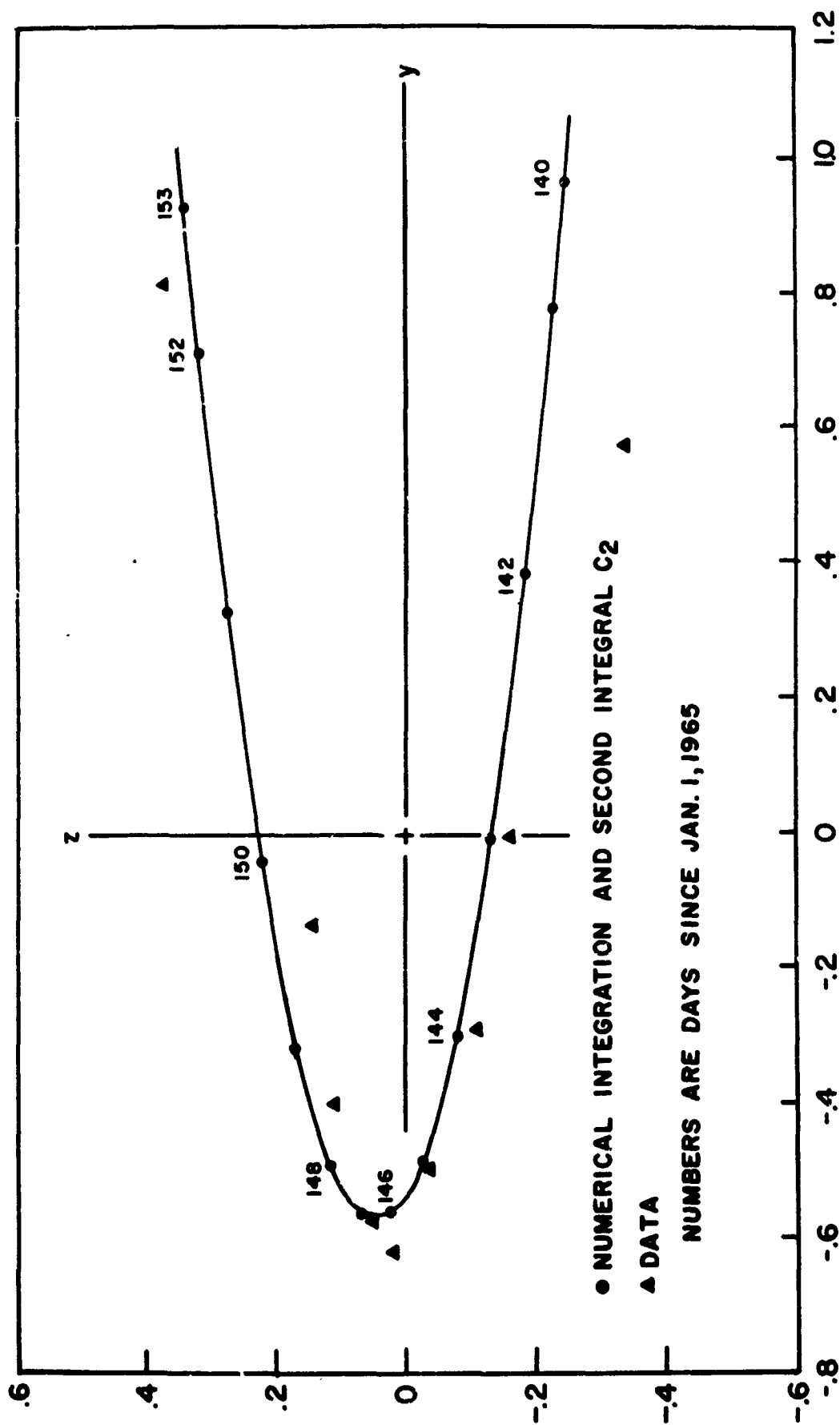


FIGURE 30. MOTION OF THE ANGULAR MOMENTUM VECTOR IN THE z, y PLANE

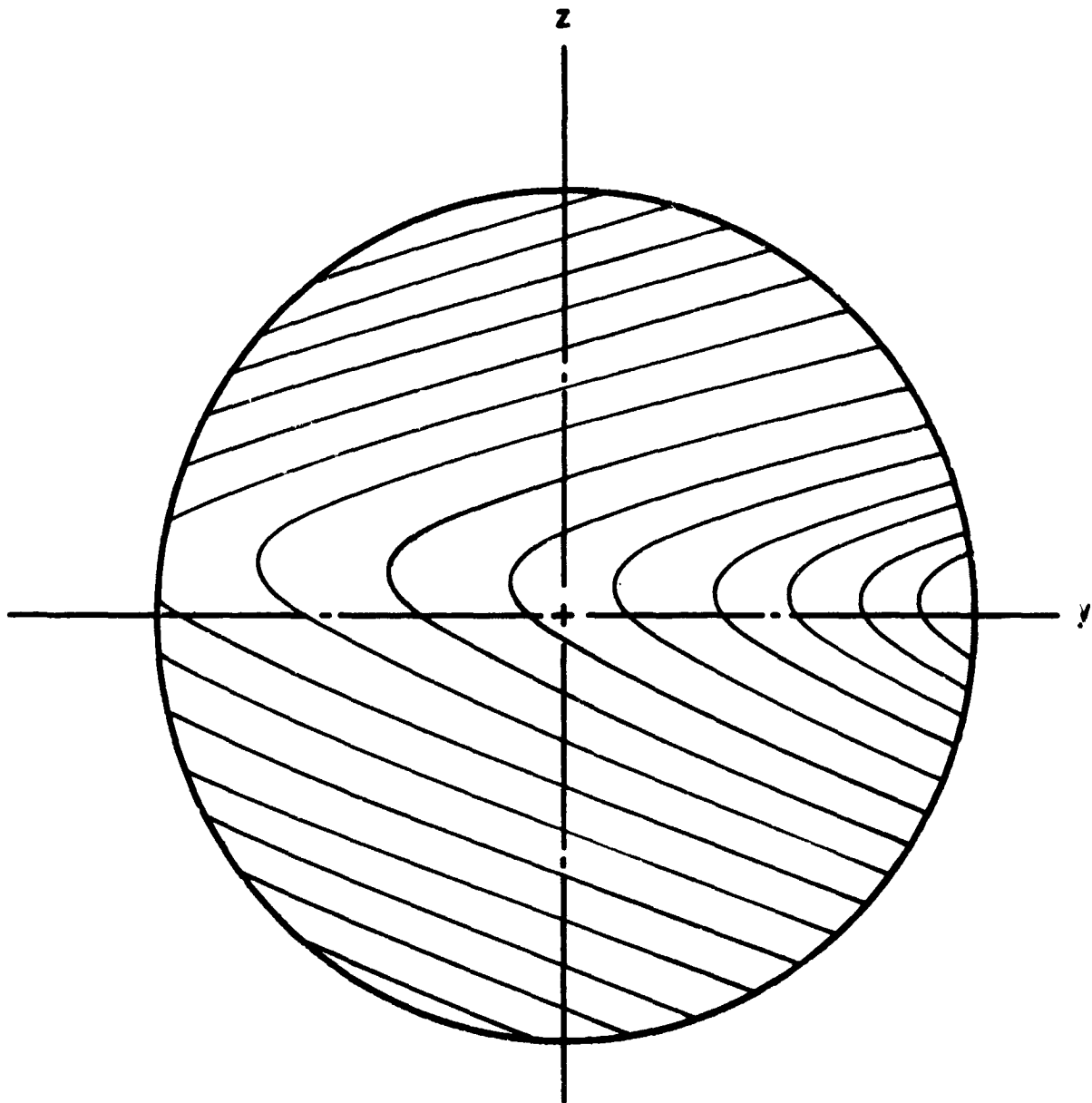


FIGURE 31. CONCEPTUAL SKETCH OF POSSIBLE PATHS OF MOTION OF THE ANGULAR MOMENTUM VECTOR IN THE z, y PLANE

ELECTRONICS OPERATION

The electronic subsystems of the three Pegasus satellites and the overall Pegasus electronic system are illustrated in Figure 32. Two years or more of operation by each satellite without any loss of prime experiment data due to electronic failures has proven that the design concept of using redundancy is of definite advantage. The value of using redundancy in the design is illustrated by noting that Table III shows that redundancy has been required in all three subsystems in which it was used. The reliability and length of operation of electronic subsystems have greatly exceeded all expectations. For example the batteries, with a life expectancy of ten months, have operated for two years or more with only one minor problem. No electronic failure has seriously degraded the performance of any Pegasus satellite. The most significant failure has resulted only in the intermittent loss of the housekeeping data of Pegasus II.

There are approximately 90 major electronic subassemblies in each of the three satellites. Hence, in the three satellites there are some 270 major electronic subassemblies of which only 10 have failed. This extremely low number of failures is even more interesting when one considers the complexity of the equipment and the number of components in some of the subsystems. For example, each satellite contains a magnetic core memory which utilizes 30 080 magnetic cores plus associated read-and-write electronics. A test has recently been completed to test every core on each satellite; not a single failure of either the cores or their electronics was detected. This fact may very well influence the data-gathering techniques used on future spacecraft.

Experience with Pegasus I resulted in adding burn-out, blow-out and disconnect circuitry to the meteoroid detector panels for Pegasus II and III. If a meteoroid impact causes a detector panel to short, an attempt is made to return the panel to operational status by applying a high current to the shorted area and thereby burning out the short. This has proved to be a very worthwhile addition.

Throughout the entire history of the space program the question of just how the space environment affects electronic systems has constantly been explored. However, since it is impossible to completely simulate the space environment, engineers and experimenters are not entirely confident in the artificially produced environmental effects on their systems. The three Pegasus

TABLE III. OPERATIONAL STATUS OF ELECTRONIC SUBSYSTEMS FOR
PEGASUS SATELLITES I, II, AND III

Electronic Subsystem	Pegasus I			Pegasus II			Pegasus III		
	Status	Are Redundant Subsystems Operating?	Status	Status	Are Redundant Subsystems Operating?	Status	Status	Are Redundant Subsystems Operating?	Are Redundant Subsystems Operating?
Power	Normal	Yes - Zener String and Main Battery Charger	Normal	Normal	Yes - Zener String	Both Zener Strings Cut-String Subsystem is Operational	Yes - Zener String	Yes - Zener String	Yes - Zener String
	Two Radiation Panels Inoperative	No	Two Current Recharge Amplifiers Intermittent	Two Current Recharge Amplifiers Intermittent	Yes - Current Recharge Amplifiers	Normal	NO	NO	NO
Communication	Normal	No	Operational Pam Data Loss	Operational Pam Data Loss	No	Normal	Yes - FM Transmitter	Yes - FM Transmitter	Yes - FM Transmitter
Temperature	Normal	N/A	Three Sensors Intermittent	Three Sensors Intermittent	N/A	Normal	N/A	N/A	N/A
Radiation	Normal	N/A	Normal	Normal	N/A	Normal	N/A	N/A	N/A
Attitude	Normal	N/A	Normal	Normal	N/A	Normal	N/A	N/A	N/A

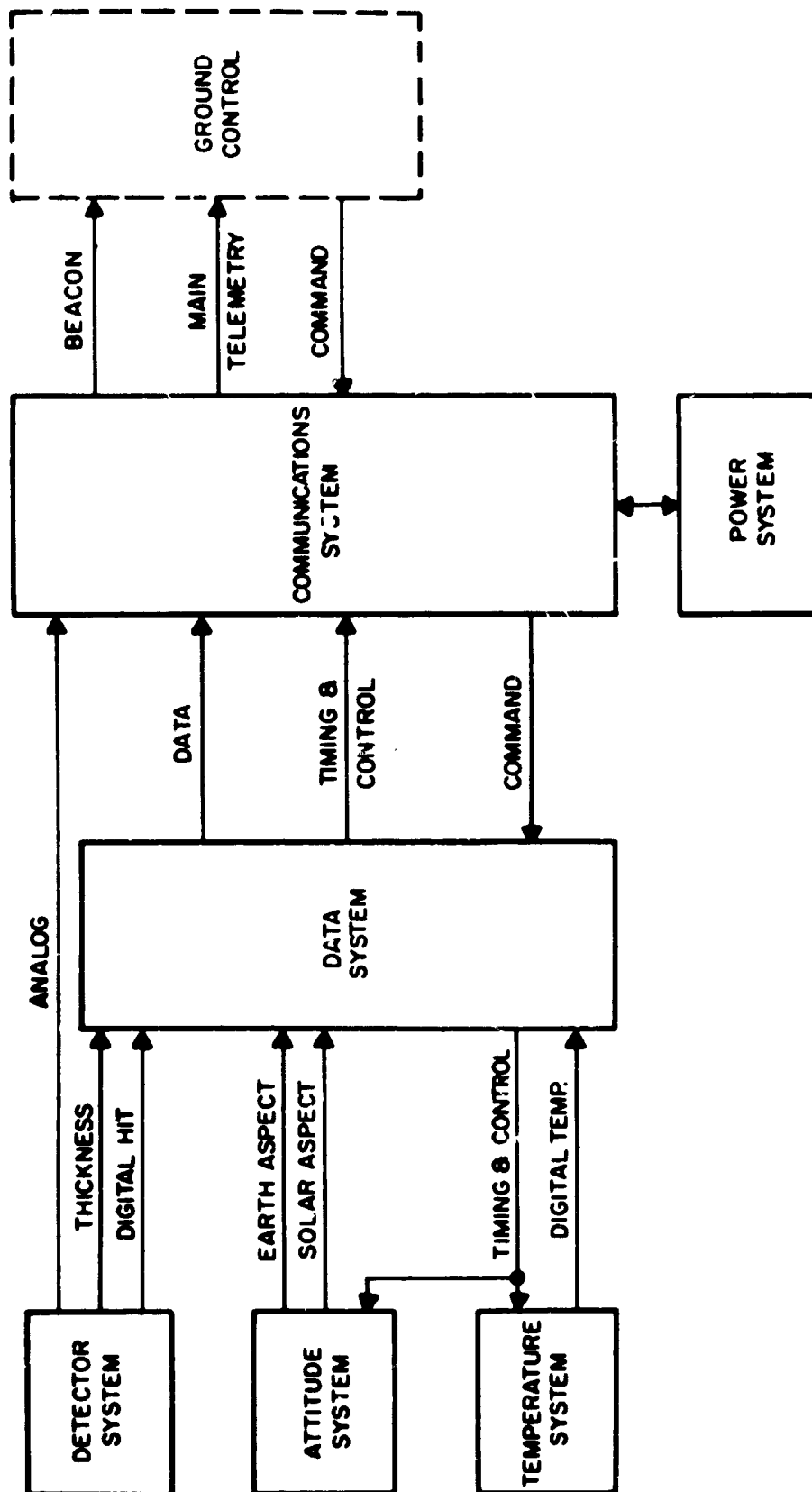


FIGURE 32. PEGASUS ELECTRONIC SYSTEM

satellites offer an excellent opportunity to study such effects since the combined number of systems make a statistically meaningful sample size. At the present time a statistical evaluation of the failures is being undertaken. The information provided by the PAM channels is being plotted in time series form and such factors as long-term trends, cyclical variations, and seasonal variations are being considered for each system. In addition, an attempt to find certain cross-correlation information is under way.

In order to provide some details on the relatively few electronic failures experienced thus far on the three Pegasus satellites, the failures will be briefly discussed. One problem common to all three satellites is failure of the Zener regulator system used to recharge the batteries from the solar panels. These failures were not altogether unexpected, since the Zeners are operated nearer their rated load than the other components are. Failure of the Zener string results in increased power being dissipated in the electronics canister and a corresponding increase in canister temperature. The increase in canister temperature is expected to shorten the life of electronic components in the canister, but is not a serious problem at this time.

Pegasus I

1. The Zener shunt regulator "A" series string went out of tolerance on December 13, 1965, causing the solar bus voltage to exceed the desired level. The redundant Zener shunt regulator "B" series string was selected and is operating normally.

2. The current limiter in the "A" Battery Charger failed on May 17, 1966. The consequent heavy charge rate caused the battery temperature to rise. Battery "B" was selected and is performing normally.

3. On May 17, 1966, a short in one battery cell caused the Battery "B" voltage to drop from its normal 29 volts to 27. There has been no additional decrease in battery voltage and no adverse effect on system operation.

Pegasus II

1. The Zener shunt regulator "A" series string went out of tolerance on October 12, 1965, causing the solar bus voltage to exceed the desired level. The redundant Zener shunt regulator "B" series string was selected and is operating normally.

2. The temperature sensors on the top-Y Solar Panel, the side +Z Solar Panel, and the side -Z Solar Panel are operating intermittently, resulting in the loss of some housekeeping data.

3. The PAM (analog) housekeeping data became intermittent on May 28, 1965, resulting in loss of approximately 75 percent of the housekeeping data.

This is attributed to a dirty connector causing loss of sync pulses to the PAM commutator. This connector fault is attributed to exposure to rain while the launch vehicle was on the pad just prior to launch.

Pegasus III

1. The Zener shunt regulator "B" series string went out of tolerance on January 18, 1966, causing the solar panel voltage to rise from the nominal regulated 42 volts to maximums exceeding 50 volts. The redundant Zener shunt regulator "A" series string was selected and operated normally until August 2, 1966, at which time a Zener shorted, resulting in a low solar panel output voltage. The Zener shunt regulator "B" series string was selected. On February 2, 1967, elevated temperatures were experienced in the batteries, the battery controller, and the power distribution unit. The Zener shunt regulator "A" series string was selected; it operated intermittently for approximately 20 hours, then assumed the failed characteristics of the "B" series string.

2. On February 11, 1966, the Number 2 FM transmitter failed. Normal voltages were being supplied to the transmitter, but there was no output. This transmitter has since operated intermittently. The redundant transmitter has operated normally.

3. The PAM housekeeping data indicate that the 28-volt subsystem voltage drops to zero at times. The memory content was checked on several days when the PAM data indicated low subsystem voltage, and in each case contained some incorrect data. This problem is presently attributed to the batteries being switched during a dark portion of the orbit. The investigation is continuing. The frequency of this problem is not known because of the low probability of detecting it with the PAM data.

A summary of the operational status of all electronic subsystems for Pegasus I, II, and III is shown in Table III.

George C. Marshall Space Flight Center
National Aeronautics and Space Administration
Huntsville, Alabama July 7, 1967

REFERENCES

1. The Meteoroid Satellite Project Pegasus, First Summary Report. NASA TN D-3505, Marshall Space Flight Center, November 1966.
2. Naumann, R. J. : The Near-Earth Meteoroid Environment. NASA TN D-3717, November 1966.
3. Bjork, R. L. : Analytical Study of Impact Effects as Applied to the Meteoroid Hazard. Contract NASw-805, Shock Hydrodynamics, Inc. , Sherman Oaks, California, September 1966.
4. Hull, W. C. ; Fleming, F. W. ; Scott, J. L. ; and Smith, L. R. : Experimental Hypervelocity Impact Research. Contract NAS8-20345, Hayes International Corp. , Birmingham, Alabama, March 1967.
5. Scully, C. N. : Experimental Hypervelocity Impact Research. Contract NAS8-21007, North American Aviation, Inc. , January 1967.
6. Jeslis, J. : Appendix K6108-9, Experimental Hypervelocity Impact Research Program. Contract NAS8-20337, May 1967.
7. Naumann, R. J. : Preliminary Calibration Results of Pegasus and Explorer XIII Meteoroid Experiments. NASA TM X-1413, June 1967.
8. The Temporal and Spatial Dependence of the Starfish Belt Electrons in 1965 and Early 1966. Paper presented at the American Geophysical Union Meeting, Washington, D. C. , April 1967.
9. Holland, Robert L. : A First Order Theory and Applications for the Rotational Motion of a Triaxial Rigid Body Orbiting on Oblate Primary. M.A. Thesis, University of Alabama, 1967.

July 3, 1967

NASA TMX-53629

APPROVAL

SCIENTIFIC RESULTS OF PROJECT PEGASUS INTERIM REPORT

Space Sciences Laboratory

The information in this report has been reviewed for security classification. Review of any information concerning Department of Defense or Atomic Energy Commission programs has been made by the MSFC Security Classification Officer. This report, in its entirety, has been determined to be unclassified.

This report has also been reviewed and approved for technical accuracy.



ERNST STUHLINGER

Director, Space Sciences Laboratory

DISTRIBUTION

INTERNAL

DIR

Dr. Wernher von Braun
Mr. James T. Shephard

DEP-T

Mr. Eberhard Rees

DEP-A

Mr. David H. Newby

I-DIR

General E. O'Connor
Mr. Hans Hueter
Mr. William Mrazek

I-K

Mr. Brian O. Montgomery
(Col., USA, Ret.)

I-1/1B-MGR

Col. William Teir

I-K-1/1B

Mr. Thomas J. Lee

I-MO-MGR

Dr. Fridtjof Speer
Mr. H. F. Kurtz

I-1/1B-S1/1B

Mr. Arthur W. Thompson

I-V-MGR

Dr. Arthur K. Rudolph

R-DIR

Mr. Hermann K. Weidner
Mr. Richard W. Cook

R-AS-DIR

Mr. Frank L. Williams (2)

R-AS-P

Mr. James A. Belew

R-AS-S

Mr. Konrad K. Dannenberg

R-AERO-DIR

Dr. Ernst D. Geissler
Mr. Otha C. Jean

R-AERO-T

Mr. William D. Murphree
Mr. Robert E. Lavender

R-AERO-Y

Mr. William W. Vaughn
Mr. Charles C. Dalton
Mr. Robert E. Smith

R-AERO-F

Mr. James P. Lindberg, Jr.

R-ASTR-DIR

Dr. Walter Haeussermann
Mr. Otto A. Hoberg
Mr. William P. Horton

R-ASTR-B

Mr. Roy E. Currie, Jr.

R-ASTR-IM

Mr. Charles T. Paludan

R-ASTR-IR

Mr. Thomas A. Barr

DISTRIBUTION (CONT'D)

R-ASTR-IRT

Mr. John G. Gregory
Mr. William H. Edens, Jr.

R-P&VE-DIR

Dr. William R. Lucas
Mr. Hans R. Palaoro

R-ASTR-M

Mr. Josef Boehm
Mr. Helmuth Pfaff
Mr. Duane N. Counter

R-P&VE-M

Mr. Lowell K. Zoller
Mr. James Kingsbury
Mr. Eugene C. McKannon

R-COMP-DIR

Dr. Helmut Hoelzer
Mr. Charles L. Bradshaw

R-P&VE PTD

Mr. George D. Hopson
Mr. R. D. Wegrich

R-COMP-RR

Mr. Roy J. Cockran
Mr. David G. Aichele

R-P&VE-P

Mr. Robert Devenish

R-COMP-RRF

Mr. Ronald L. Neece
Mr. Freddie A. Rodrigue

R-Qual-DIR

Mr. Dieter Grau

R-COMP-RRG

Mr. Paul O. Hurst

R-SSL-DIR

Dr. Ernst Stuhlinger
Mr. Gerhard Heller
Mr. George C. Bucher

R-COMP-PRO

Mr. George T. Jarret

R-SSL-X

Mr. Hugh J. Dudley
Dr. Alfred H. Weber

R-COMF-CSC

Mr. E. Allen

R-SSL-C

Mr. James A. Mathis
Reserve (10)

R-EO

Dr. William G. Johnson (3)
Miss Mary Jo Smith

R-SSL-P

Dr. James B. Dozier
Mr. Ray V. Hembree
Mr. Harvell P. Williams
Mr. William Chisholm

R-OM-DIR

Colonel Walter S. Fellows

R-SSL-PM

Mr. Robert J. Naumann
Mr. Kenneth S. Clifton
Mr. Patrick N. Espy

R-ME-DIR

Mr. Werner R. Kuers
Mr. Hans F. Wuencher

DISTRIBUTION (CONT'D)

R-SSL-PA

Mr. Robert L. Holland
Mr. Matthew W. Barkley, Jr.

R-SSL-N

Dr. Russell D. Shelton
Mr. Eugene W. Urban
Mr. Richard A. Potter

R-SSL-T

Mr. William Snoddy
Mr. Edgar R. Miller
Mr. Charles Schafer
Mr. Roger Linton
Mr. Tommie C. Bannister

R-SSL-S

Mr. James A. Downey, III

R-TEST-DIR

Mr. Karl L. Heimburg

R-TEST-I

Dr. Werner H. Seiber

R-TEST-ID

Dr. Helmut G. Lackner

PA

Mr. Bart Slattery

CC-P

MS-H

MS-IP

MS-IL (8)

MS-T (6)

I-RM-M

EXTERNAL DISTRIBUTION

National Aeronautics & Space Administration
Washington, D. C. 20546

A Mr. James E. Webb

AD Dr. Robert C. Seamans, Jr.

M Dr. George E. Mueller

MA Maj. Gen. Samuel C. Phillips
Mr. Lee B. James (Col., USA, Ret.)

MAT Mr. James Saunders, Jr.

MTD Mr. Douglas R. Lord

MTY Dr. Franklin P. Dixon

MLD Mr. John H. Disher

MT Mr. George B. Trimble

MTE Mr. Maurice J. Raffensperger

ML Mr. Charles W. Mathews

MO Major General John O. Stevenson
(USAF, Ret.)

S Dr. Homer E. Newell

SG Dr. Maurice Dubin
Mr. Jesse L. Mitchell
Dr. Henry J. Smith
Dr. Nancy G. Roman

DISTRIBUTION (CONT'D)

R	Dr. Mac C. Adams	JET PROPULSION LABORATORY
		4800 Oak Grove Drive
RRA	Dr. Raymond H. Wilson, Jr.	Pasadena, California 91103

RV	Mr. Milton B. Ames, Jr.	10	Dr. William H. Pickering
----	-------------------------	----	--------------------------

RV-1	Mr. E. O. Pearson	271	Dr. Leonard D. Jaffe
------	-------------------	-----	----------------------

Mr. J. W. Keller

	Mr. C. T. D'Aiutolo	294	Dr. Royce R. Marshall
--	---------------------	-----	-----------------------

AMES RESEARCH CENTER
Moffett Field, California 94035

JOHN F. KENNEDY SPACE CENTER
Kennedy Space Center, Florida 32899

MS 200-4	Dr. H. Julian Allen
----------	---------------------

AA	Dr. Kurt H. Debus
----	-------------------

MS-204-2	Dr. Charles P. Sonett
----------	-----------------------

PB	Dr. Rudolf H. Bruns
----	---------------------

MS 204-3	Dr. Donald E. Gault
----------	---------------------

JA	Dr. Hans F. Gruene
----	--------------------

MS 223-1	Mr. James L. Summers
	Mr. C. Robert Nysmith

HA	Col. Rocco A. Petrone
----	-----------------------

MS 210-4	Mr. Bedford A. Lampkin
----------	------------------------

LANGLEY RESEARCH CENTER
Hampton, Virginia 23365

ELECTRONICS RESEARCH CENTER
575 Technology Square
Cambridge, Massachusetts 02139

MS 106	Dr. Floyd L. Thompson
--------	-----------------------

MS-213	Mr. Herbert A. Wilson, Jr.
--------	----------------------------

D	Dr. Winston E. Kock
	Mr. W. S. Cashman

MS 212A	Mr. Don D. Davis, Jr.
---------	-----------------------

GODDARD SPACE FLIGHT CENTER
Greenbelt, Maryland 20771

MS 217	Mr. William H. Kinard
	Mr. Robert L. O'Neill

MS 215	Mr. Earl C. Hastings, Jr.
--------	---------------------------

Code 100	Dr. John F. Clark
----------	-------------------

LEWIS RESEARCH CENTER
Cleveland, Ohio 44135

Code 513	Mr. Robert L. Mitchell
----------	------------------------

Code 613	Dr. Carl S. Nilsson
	Mr. Otto E. Berg

MS 3-2	Dr. Abe Silverstein
--------	---------------------

MS 7-1	Mr. Irvin J. Loeffler
--------	-----------------------

DISTRIBUTION (CONT'D)

MANNED SPACECRAFT CENTER
Houston, Texas 77058

AA Dr. Robert R. Gilruth

RL Mr. William E. Davidson

EA5 Mr. Warren Gillespie

TG Mr. Paige B. Burbank
 Mr. Burton Cour-Palais
 Mr. Thomas W. Lee

Scientific and Technical Information
Facility (25)
P. O. Box 33
College Park, Maryland 20740
Attn: NASA Representative (S-AK/RKT)

Dr. C. L. Hemenway
The Dudley Observatory
140 South Lake Avenue
Albany, New York 12208

Dr. F. L. Whipple
Director
Smithsonian Astrophysical Observatory
60 Garden Street
Cambridge, Massachusetts 02138

Dr. C. A. Lundquist
Assistant Director
Smithsonian Astrophysical Observatory
60 Garden Street
Cambridge, Massachusetts 02138

Dr. J. D. Wray
Director
Institute of Meteoritics
University of New Mexico
Albuquerque, New Mexico 87106

Dr. J. A. Hynek
Northwestern University
Evanston, Illinois 60201

Dr. P. M. Millman
National Research Council of Canada
McGill University
Ottawa Ontario, Canada

Dr. G. S. Hawkins
Associate Prof. of Astronomy
Director of the Observatory
Harvard College Observatory
Cambridge, Massachusetts 02138

Mr. B. A. Rhodes
Rhodes & Bloxsom
7343 Deering Avenue
Canoga Park, California 91303

Dr. J. H. Johnson
Research Center, Ling-Temco-Vought
Dallas, Texas 75201

Dr. C. M. Askey
Hayes International
Birmingham, Alabama

Mr. G. T. Schjedahl
G. T. Schjedahl Co.
Northfield, Minnesota

Mr. E. Uhl
President, Fairchild Hiller Co.
Hagerstown, Maryland

Dr. Douglas Duke
Box 9115
University of Miami
Coral Gables, Florida 33124

DISTRIBUTION (CONCLUDED)

**Mr. Robert B. Morse
Ball Brothers Research Corporation
Box 1062
Boulder, Colorado 80302**

**Mr. R. L. Bisplinghoff
Department of Aeronautics & Astronautics
Massachusetts Institute of Technology
Cambridge, Massachusetts 02139**